




**Magnetic stability of Ce and Nd single atom magnets on insulating MgO/Ag(100)**Yaqing Chen,<sup>1</sup> Jie Liu ,<sup>1</sup> Meng Ju,<sup>1</sup> Ruizhi Qiu ,<sup>2,\*</sup> and Hongkuan Yuan <sup>1,3,\*</sup><sup>1</sup>*School of Physical Science and Technology, Southwest University, Chongqing 400715, China*<sup>2</sup>*Institute of Materials, China Academy of Engineering Physics, Mianyang, Sichuan 621907, China*<sup>3</sup>*Chongqing key Laboratory of Micro&Nano Structure Optoelectronics, Southwest University, Chongqing 400715, China*

(Received 17 December 2022; revised 11 May 2023; accepted 20 June 2023; published 28 June 2023)

Surface supported lanthanide single-atom magnets (SAMs) with thermal stability and long magnetic lifetime offer the possibility for the usage of atomic magnetic data storage. Theoretically identifying the factors that prohibit the quantum tunneling of magnetization (QTM) and maximize the magnetic anisotropy energy (MAE) are essential to design novel atomic magnets. The density function theory (DFT), the simulated x-ray absorption, and magnetic circular dichroism spectra as well as crystal field (CF) model Hamiltonians were employed to investigate the electronic structure and magnetic properties of early lanthanide adatoms (Ce, Nd) adsorbed on the MgO/Ag(100) surface. We identified that they can be stably positioned on O atom of MgO surface by strong ionic bond as well as a certain covalent bond via the hybridization between Ce/Nd-5*d* with O-2*p* orbitals. Our DFT calculations with multiplet simulation reveal that the 4*f* occupancies of these adatoms are essentially identical to that of freestanding atoms. The expectation values of spin/orbital magnetic moments are evaluated as  $-0.72/2.86 \mu_B$  for the ground states  $|J = 5/2, J_z = \pm 5/2\rangle$  of Ce adatom, yet almost quenched values for the ground-state doublet of Nd adatom due to a mixture of  $|J = 4, J_z = \pm 4\rangle$  states within equal weights. Although the QTM between the degenerate ground states is prohibited for Ce@MgO/Ag(100), the spin-flip excitations from  $|J = 5/2, J_z = \pm 5/2\rangle$  ground state to  $|J = 5/2, J_z = \pm 3/2\rangle$  first excited state followed by the subsequent deexcitation reduce the magnetization reversal barrier from  $U_{\text{rev}} = 4.17$  meV to 2.87 meV. This energy barrier still guarantees a long magnetic lifetime estimated to be 239 s at 10 K. For Nd@MgO/Ag(100), direct QTM between the degenerate states  $|J = 4, J_z = \pm 4\rangle$  results in the fast magnetization reversal process without energy barrier and leads to magnetic instability.

DOI: [10.1103/PhysRevB.107.214444](https://doi.org/10.1103/PhysRevB.107.214444)**I. INTRODUCTION**

The single-atom magnets (SAMs) provide a promising opportunity in realizing the atomic scale data storage of classical information in quantum spin and miniaturizing the magnetic storage devices [1–6]. When considering magnetic recording in the quantum limit, the inherent dilemma is keeping SAMs in one of two stable ground states so as to guarantee a finite magnetic moment and thus magnetic hysteresis above a certain blocking temperature. The absence of quantum tunneling of magnetization (QTM) is the precondition for achieving this requirement at zero-applied magnetic field [5–15]. Even if the two ground states are protected from QTM, it should be considered how their exchange coupling to the electrons of the substrate affects their capability to store a classical bit [11]. In fact, the magnetic stability of the ground states depends crucially on the key quantity of magnetic anisotropy energy (MAE), which is conventionally defined as an “energy barrier” required in switching the magnetization by the thermally assisted fluctuation. Correspondingly, large MAE can protect the magnetic moment in a specific orientation and undoubtedly reduce the probability of spontaneous reversal of magnetization at high temperature. For quantum

spins, total zero-field splitting (TZFS) energy between the highest- and lowest-lying states is regarded as the MAE, and even more impressively, energy difference between the ground state and the first excited state is related with the effective anisotropy barrier  $U_{\text{rev}}$  for magnetic reversal [4]. This means that large MAE (TZFS) is not the only necessary condition for stabilizing the magnetic state of SAMs [9], because the magnetization reversal does not necessarily climb over the full MAE profile due to the QTM or the spin-flip excitation transition, i.e., the underbarrier magnetic relaxation pathways would reduce the MAE to an effective barrier  $U_{\text{rev}}$ .

Transport pump and probe techniques with spin-polarized tips permit measuring the spin-relaxation time. In seeking for the slow-relaxing SAMs, the critical strategy is to maximize the MAE and at the same time to minimize the underbarrier relaxation pathways, namely, the decoupling of magnetic states from the scattering of the conduction electrons and vibrational phonon of the substrate [16]. The question of how to integrate an excellent magnetic adsorbate and compatible substrate in achieving these objectives has remained a continuing topic. In early 2003, large orbital moments and giant MAE were pioneeringly realized for single Co atom deposited on metallic Pt(111) surface by the x-ray absorption (XAS) and magnetic circular dichroism spectra (XMCD) measurements [1]. Motivated by the search for elemental adatoms with large MAE, following theoretical calculations based on density function

\*Corresponding authors: qiuruizhi@caep.cn; yhk10@swu.edu.cn

theory (DFT) have implemented a huge enthusiasm on  $3d$ ,  $4d$ , and  $5d$  transition-metal (TM) atoms deposited on non-magnetic substrate (see Refs. [17–31] and references therein). With the recent development of single atom spin detection technologies such as scanning tunneling microscopy (STM) and inelastic scanning tunneling spectroscopy (ISTS) as well as local electronic structure and magnetic probe technologies of XAS and XMCD for a quite low-surface coverage, the experimental realization and characterization were dominantly pursued on Fe, Co, Ni adatoms [32–35]. While most TM SAMs show large local magnetic moments and giant MAEs, the fundamental problem is the fast QTM in experiments, because their magnetic ground states are significantly destabilized by the spin-flip scattering with the substrate conduction electrons [36–39]. Even as thickness of the insulating film are changed, the observed lifetimes remain short [40]. For example, single Co adatom on MgO(100) layer has been revealed to break the MAE record to show 58 meV, but no magnetic remanence has been experimentally detected due to insufficient amount of time for a fixed magnetic orientation [3].

From the point of view of the magnetic adsorbate, lanthanide (Ln) adatoms display a remarkable advantage over TM adatoms owing to the special characteristic of  $4f$  electrons: (i)  $4f$  orbitals are strongly localized (shielded by the suborbitals  $5p^66s^2$ ) and hybridized weakly with the substrate, making  $4f$  magnetic moments rarely disturbed by the conduction electrons and potentially having longer magnetic relaxation lifetimes [41,42]; (ii) spin-orbital coupling (SOC) of  $4f$  electrons is at least an order of magnitude higher than crystal field (CF) [43], making total angular momentum  $J$  together with its projection  $J_z$  be the good quantum numbers, and consequently strong SOC gives rise to large magnetic anisotropy splitting of degenerate magnetic states [44]. Since  $U_{\text{rev}}$  can be associated with the first excitation energy [45,46], large energy splitting may give long magnetic relaxation time in according to Arrhenius-like behavior  $\tau = \tau_0 e^{U_{\text{rev}}/k_B T}$  [9,41,42]; (iii) large uniaxial magnetic anisotropy  $D$  possessed by  $4f$ -based single ion, on the same argument, demonstrates the large  $U_{\text{rev}}$  of Ln atoms in terms of  $U_{\text{rev}} = DJ^2$  [47,48]. From the point of view of substrate, three decisive factors can be addressed: (i) a thin insulating layer should be introduced to decouple the interactions of magnetic adatom from substrate conduction electrons for suppressing the spin-flip scattering [6,7]; (ii) vibration frequency of high-stiffness substrate should decouple from the first available spin transition of magnetic adatoms to hinder the spin-phonon coupling or the phonon dissipation in the spectral range close to the spin excitations [5,16]; and (iii) suitable local CF symmetry should match with the total angular momentum  $J$  of adatom to prevent the direct QTM between the ground state doublet and the spin-flip transition between the ground state and the excited states [43]. So far, such a combination to enhance  $U_{\text{rev}}$  and to increase magnetic relaxation time has produced some success. For example, long-lived magnetic quantum states without QTM were read and wrote on the time scale of 1500 s at 10 K temperature for Ho atom individually adsorbed on MgO(100) insulating thin films [5,6,16]. Among the series of the Ln-based SAMs, the late Ln adatoms on different thin insulating layers such as Ln@MgO (Ho [5,6,16,49–52],

Gd [53], Dy [10,54,55]), Ln@graphene/Ir(111) (Ln = Sm, Eu, Dy, Ho, Tb, Er, Tm) [7,9,56–58], Dy@graphene/Cu(111) [59], Ln@Cu<sub>2</sub>N/Cu (Ln = Tm, Lu) [60] are being pursued in recent experiments, where the large out-of-plane magnetic moment, higher MAE and long magnetic lifetimes were often derived. At the same time, the late Ln adatoms such as Gd, Er, Ho, Dy, Tm individually deposited on clean metal/semiconductor solid surfaces attracted a lot of experimental attention [61–64]. If the ground-state angular momentum  $J_z$  of Ln adatom is compatible with the specific symmetry of Ln adsorption site, the symmetry will prohibit the QTM and suppress the substrate-driven relaxation [4]. It has been found that Ho SAM has  $U_{\text{rev}} = 8$  meV excitation energy and longer lifetime of 729 s, even though the magnetic ground states ( $|J = 8, J_z = \pm 8\rangle$  vs  $|J = 8, J_z = \pm 6\rangle$ ) as well as the magnetic signature (appearance vs absence of magnetization hysteresis) are an ongoing debate [4,49,61].

In spite of abundant experimental achievements and proposed phenomenological interpretations in theory, an overarching model to capture the essential ingredients causing magnetization reversal and to explain the magnetic relaxation of Ln SAMs is insufficient. Firstly, previous studies were limited to the late Ln adatoms, especially for the depositions on MgO thin film from the experimental side, and an open research area should be to expand such studies to the early Ln adatoms such as Ce and Nd, motivated by Ho adatom being the first experimentally found SAMs [5]. Understanding the magnetic stability of whole period Ln adatoms would be helpful to design new Ln-based SAMs with even slower magnetic relaxation. Moreover, the  $4f$  magnetic moment of an individual Ce adatom has been sensed by a detector spin at the apex of a functionalized STM tip but the anisotropy energy with the favoring magnetization direction is not yet fully known [65]. In addition, Delgado *et al.* [11] have found that fundamental differences exist between integer and semi-integer spins for both reading and recording classical information in a quantized spin, and they pointed out that two magnetic ground states with opposite magnetization appear only in the case of semi-integer spins owing to forbidden QTM. Motivated by these findings, the effect of half-integer  $J$  (Ce@MgO) and integer  $J$  (Nd@MgO), together with the symmetry constraint on QTM and spin-flip transitions, have been comparatively studied. Typically, we proposed a strategy to achieve stable magnetization based on the first principles and CF Hamiltonian calculations. We combined the SOC-DFT calculation, multiplet simulation with the CF model Hamiltonian to determine the spin and orbital magnetic moment, energy spectrum, magnetic stability, and magnetic relaxation time. The adsorption site, structural stability, and electronic features are also explored. We provide a complete and rigorous map of the combinations of symmetries and total angular momentum to rationalize the magnetic reversal mechanisms. We show that the MAEs are in semiquantitative agreement with the TZFS obtained from the solutions of multiplet simulation and the CF model Hamiltonians. The organization of this paper is as follows. In Sec. II, theoretical background for DFT calculations, multiplet simulation, and CF model calculations are outlined. We discuss the results in Sec. III. and conclusions are given in Sec. IV.

## II. THEORETICAL METHOD

### A. DFT calculation

We performed the spin-polarization DFT calculations with Perdew-Burke-Ernzerhof for generalized gradient approximation (GGA-PBE) [66] as implemented in OpenMX software [67]. Our formalism was based on the nonorthogonal linear combination of localized pseudoatomic orbitals (LCPAO) [68,69]. The radial cutoffs for the pseudoatomic orbitals are 8.0, 6.0, 9.0, and 7.0 a.u. for Ln, O, Mg, and Ag, respectively. The cutoff energy of 450 Ry was used to expand wave functions in a plane wave basis set. The Monkhorst-Pack (MP) [70]  $k$ -point grids of  $7 \times 7 \times 1$  was used for the geometry optimization and  $14 \times 14 \times 1$  for the electronic structures calculation. It is well known that strong correlation effect of the localized  $4f$  electron plays a key role in determining the properties of Ln atoms; however, the conventional DFT methods cannot deal with the strongly correlated systems well. This limitation can be solved by introducing Hubbard parameter  $U$  combined with exchange interaction  $J$  for the  $4f$  electrons [71,72]. Here, effective values of  $U_{\text{eff}} = U - J$  confirmed by Larson *et al.* [73] were employed. The van der Waals (vdW) interaction described by the DFT-D2 method has been adopted in structural optimizations since it is important for the absorption of Ln atoms in MgO films [74]. The atoms were fully relaxed without any symmetric constrains during the optimization process. For calculating the spin and orbital moments and MAE, the SOC was included by performing GGA+ $U$ +vdW+SOC calculations on different magnetization orientations. High energy convergence criteria of  $10^{-7}$  Hartree was set for the self-consistent field procedure and the maximum residual force on each atom was less than  $10^{-4}$  Hartree/Bohr.

### B. Multiplet simulation

To gain insight into the origin of the remarkable magnetic stability and MAE, we carried out multiplet simulations using the MultiX code [75]. The calculations were performed with the aim of producing the magnetic energy splitting spectrum, XAS and XMCD spectra. Our multiplet simulation is based on the CF environment and incidence angle of x-rays on the magnetic atom. The CF generated by the interaction of Ln atom with MgO/Ag(100) substrate was modeled with point charges. For the highly localized  $4f$  states of Ln atoms, this description was well justified due to their mainly electrostatic interaction with the substrate [76]. The sign and values of point charge represent the deviation from the spherical charge distributions of each isolated atom around the Ln adatom [9]. The atomic positions were obtained by DFT calculations and the strength of atomic charges have made some properly adjusting. To identify the magnetic easy axis, we implemented XAS and XMCD simulations at two incident angles, i.e., normal incidence angle ( $\theta = 0^\circ$ ) and grazing incidence angle ( $\theta = 90^\circ$ ). All measurements were performed by varying the energy of the incident x-rays with the  $M_{4,5}$  adsorption edges, which are  $3d \rightarrow 4f$  transitions.

### C. CF model calculations

For the Ln adatom, its SOC interaction is much larger compared with the CF interaction, and its magnetic behavior can

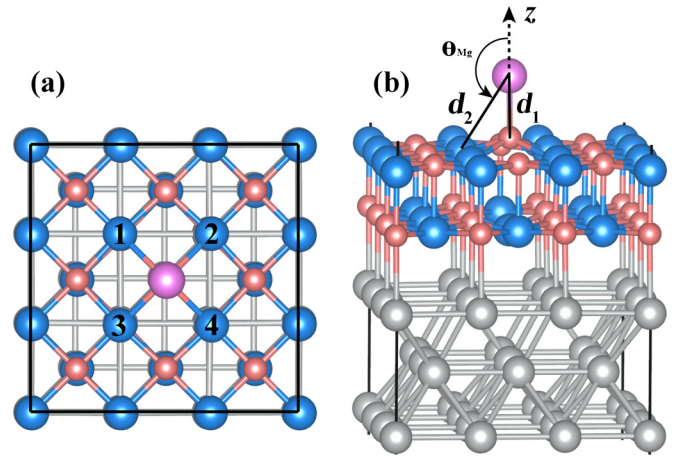


FIG. 1. Top view (a) and side view (b) of Ln-adsorbed MgO/Ag(100). Purple, pink, blue, and gray balls represent Ln, O, Mg, and Ag atoms, respectively.  $d_1/d_2$  is the distance from Ln atom to its nearest neighboring O and Mg atoms, respectively.

be described by the ground multiplet  $^{2S+1}L_J$  [77,78]. The CF symmetry and strength determined by the adsorption site of Ln atom would lift the degenerate  $J_z$  states and induce a TZFS in the multiplet. The values of TZFS have the comparable orders of magnitude with that of MAE for Ln adatom systems, providing the feasibility method by using CF splitting to estimate the MAE [79]. The general CF model Hamiltonian can be written using the Stevens operators formalism as [4]

$$H_{\text{CF}} = \sum_{n=0}^{\infty} \left( \sum_{k=0}^n B_n^k O_n^k + \sum_{k=1}^n \tilde{B}_n^k \tilde{O}_n^k \right) \quad (1)$$

where  $B_n^k$  and  $\tilde{B}_n^k$  are the anisotropy constants called CF parameters; Stevens operators  $O_n^k$  and  $\tilde{O}_n^k$  are the polynomials of order  $n$  in terms of  $J_z$ ,  $J_+$ , and  $J_-$ ; operator degree  $n$  should be even numbers constrained by the time-reversal symmetry, because those states with opposite magnetic momentum have the identical energy when the magnetic field is zero [9];  $k$  is the operator orders [80]. Note that not all terms in the expansion will affect the energy levels, as their matrix elements may yet be zero. For a vertical mirror plane presented by the surface adsorption, numerical values of  $O_n^k$  operators are obtained for  $n = 2, 4, \dots, 2J$  with  $n \geq k$ , while all conjugate operators  $\tilde{B}_n^k \tilde{O}_n^k$  cancel out each other and will vanish [81]. Three things should be emphasized by converting the above formula into an expansion polynomial: (i) the terms with  $n > 2J$  will vanish because the operators only act on the multiplet states within  $2J+1$ ; (ii) the terms with  $n > 2l$  will vanish, where  $l$  is orbital angular momentum of the open shell of magnetic atom, e.g.,  $n$  is allowed to 6 for  $4f$  orbital with  $l = 3$  because only  $n \leq 6$  terms yield nonzero matrix elements; and (iii)  $k$  ( $k \leq n$ ) is restricted to be the specific values by the CF symmetry of adsorption site, e.g., only  $k = 0, 3$  are selected under the  $C_{3v}$  symmetry if we take  $n = 4$  for  $d$  orbital, because  $k$  should be differed by multiples of 3 and the values larger than 4 such as  $k = 6, 8, \dots$  are discarded [23,50,82].

For the  $4f$ -Ln atom individually deposited on MgO surface within  $C_{4v}$ -symmetry, as shown in Fig. 1, we take  $n = 0, 2, 4, 6$  within the largest value of  $n = 2l = 6$  as well as



$k = 0, 4$  within the largest value of  $k = 4$ , respectively. More specifically,  $B_0^0 O_0^0$  term can be negligible because it contains only  $J$  that does not contribute the energy splitting. Thus, the CF model Hamiltonian is specifically expressed as [83]

$$H_{4v} = B_2^0 O_2^0 + B_4^0 O_4^0 + B_6^0 O_6^0 + B_4^4 O_4^4 + B_6^4 O_6^4. \quad (2)$$

For a given  $J$ , the Steven operators on the states of  $|J, m_j\rangle$  are given by the following formulas:

$$\begin{aligned} O_2^0 |J, m_j\rangle &= [3J_z^2 - J(J+1)] |J, m_j\rangle, \\ O_4^0 |J, m_j\rangle &= [35J_z^4 - 30J(J+1)J_z^2 + 25J_z^2 \\ &\quad - 6J(J+1) + 3J^2(J+1)^2] |J, m_j\rangle, \\ O_6^0 |J, m_j\rangle &= [231J_z^6 - 315J(J+1)J_z^4 + 735J_z^4 \\ &\quad + 105J^2(J+1)^2J_z^2 - 525J(J+1)J_z^2 \\ &\quad + 294J_z^2 - 5J^3(J+1)^3 + 40J^2(J+1)^2 \\ &\quad - 60J(J+1)] |J, m_j\rangle, \\ O_4^4 |J, m_j\rangle &= \frac{1}{2}(J_+^4 + J_-^4) |J, m_j\rangle \\ O_6^4 |J, m_j\rangle &= \frac{1}{4}[11J_z^2 - J(J+1) - 38](J_+^4 + J_-^4) \\ &\quad + (J_+^4 + J_-^4)[11J_z^2 - J(J+1) - 38] |J, m_j\rangle \end{aligned} \quad (3)$$

with operators

$$\begin{aligned} J_z |J, m_j\rangle &= m_j |J, m_j\rangle, \\ J_x |J, m_j\rangle &= \frac{1}{2}(J_+ + J_-) |J, m_j\rangle, \\ J_\pm |J, m_j\rangle &= \sqrt{j(j+1) - m_j(m_j \pm 1)} |J, m_{j\pm 1}\rangle. \end{aligned} \quad (4)$$

On the one hand, we give some comments for the Hamiltonian terms with  $k = 0$ . These terms do not mix the  $|J, m_j\rangle$  states, because the uniaxial CF operators of  $O_2^0$ ,  $O_4^0$ , and  $O_6^0$  terms contain only powers of  $J_z$  and  $J$  operators. When these terms operate on their eigenstates  $|J, m_j\rangle$ , they will partially lift the degeneracy of  $J_z$  eigenstates and yield different eigenvalues, giving the TZFS. Note that  $B_2^0$  parameter is often significantly larger than  $B_4^0$  and  $B_6^0$  parameters, and consequently  $B_2^0 O_2^0$  term will play a dominating role in splitting the energy levels. Due to the  $J_z^2$  operator of  $O_2^0$  term, a parabola energy shape would be presented along with the magnetic quantum number from  $-m_j$  to  $+m_j$ . For  $B_2^0 < 0$ , there is a pointing downward parabola, which gives the ground-state doublet within the maximal  $m_j$  and exhibits an out-of-plane anisotropy; on the contrary, for  $B_2^0 > 0$  the upward parabola will give the ground state doublet within the minimal  $m_j$ . The higher order operators like  $O_4^0$  and  $O_6^0$  terms would result in nonmonotonic distribution of  $J_z$  energy levels. They would change the square power relation determined by  $J_z^2$  operators of  $O_2^0$  term and may potentially lead to the ground-state doublet within the intermediate  $m_j$ . On the other hand, we should pay great attention to the Hamiltonian terms with  $k \neq 0$  that contain powers of  $J_+$  and  $J_-$  operators, i.e., the transverse CF operators  $O_4^4$  and  $O_6^4$ . When these terms operate on the states  $|J, m_j\rangle$ ,  $J_+$  and  $J_-$  operators would mix different  $|J, m_j\rangle$  states that have the magnetic quantum differing by multiples of 4 ( $\Delta m_j = 4$ ). This would result in several classes of new eigenstates and each class is a linear combination of several

$|J, m_j\rangle$  states. Therefore, the eigenstates of Hamiltonian are no longer pure  $|J, m_j\rangle$  states and the magnetic momentum is often be the expectation values of  $m_j$ .

*Tunneling case.* When two eigenstates of the Hamiltonian have  $\Delta m_j = 4m$ , the so-called QTM occurs via the role of transverse  $O_4^4$  and  $O_6^4$  operators, i.e., they are contributed from the nonzero matrix elements,

$$\begin{aligned} \langle J_z = J, m_j | O_4^4, O_6^4 | J_z = J, m_{j'} \rangle &\neq 0, \\ \Delta m_j &= |m_j - m_{j'}| = 4, 8, 12, 16. \end{aligned} \quad (5)$$

The maximal value  $\Delta m_j$  between  $|J, m_j\rangle$  and  $|J, m_{j'}\rangle$  eigenstates depends on the available total angular momentum  $J$  of Ln atom, where the lower  $J$  value will give less  $\Delta m_j$ . If two ground states meet the requirements of  $\Delta m_j = 4m$  (where  $m$  is an integer,  $m = 1, 2, 3, 4$ ) and possess the energy difference  $\Delta E$ , the direct QTM provided by the energy  $\Delta E$  of the tunneling electrons would enable magnetization reversal and produce two new mixture states with the quenched  $\langle J_z \rangle$ . This reduces the ‘‘ideal’’ MAE to  $\Delta E$  if the scattering from the conduction electrons cannot be inhibited, and the ground state is destabilized because a spin reversal to pass through the ‘‘ideal’’ MAE barrier is not needed.

*Spin-flip case.* Even if there is no mixing state and no allowed direct QTM between two ground states, the scattering events mediated by the exchange interaction to conduction electrons and phonons of the supporting substrate may yield the ‘‘spin-flip’’ of excitation transition by considering the selection rules, i.e., linking two ground states together via the intermediate excitation states. The contribution from nonzero matrix elements can be obtained via the formula  $v$  [84,85],

$$\begin{aligned} v &= \langle \psi_j^- | \hat{V} | \psi_j^+ \rangle, \\ \hat{V} &= \hat{J} \cdot \hat{\sigma} = J_z \sigma_z + \frac{1}{2}(J_+ \sigma_- + J_- \sigma_+), \end{aligned} \quad (6)$$

with

$$\begin{aligned} \sigma_+ |\downarrow\rangle &= 2|\uparrow\rangle, \\ \sigma_- |\uparrow\rangle &= 2|\downarrow\rangle, \\ \sigma_+ |\uparrow\rangle &= \sigma_- |\downarrow\rangle = 0, \end{aligned} \quad (7)$$

where  $\hat{J}$  and  $\hat{\sigma}$  represent angular-momentum operator of Ln atom and spin operator of tunneling electron [4], respectively;  $\hat{V}$  is the transition operator related to the scattering with a tunneling electron;  $J_+/J_-$  and  $\sigma_+/\sigma_-$  are the ladder operators of total angular momentum and spin momentum within  $J$  multiplet, respectively. To characterize the interactions of tunneling electron with localized spin, three necessary matrix elements  $\langle \psi_m^- | J_z | \psi_m^+ \rangle$ ,  $\langle \psi_m^- | J_+ | \psi_m^+ \rangle$ ,  $\langle \psi_m^- | J_- | \psi_m^+ \rangle$  should be calculated. If one of three matrix elements is nonzero, a single electron scattering event may reverse the magnetization of Ln atom via the excitation transition from  $|\pm J_z\rangle$  state to  $|J_z \pm 1\rangle$  state and then the deexcitation process to  $|\mp J_z\rangle$  state, causing a complete magnetization reversal. This would open a new spin relaxation channel via the scattering with the substrate electrons, reducing the magnetization reversal energy and shortening the spin lifetimes [86]. Otherwise, a single electron scattering event does not happen and the orientation of magnetic moment will not be reversed.

Under the electric dipole approximation for the selection rule, the quantum transitions are induced between both ground

TABLE I. The Ln-O and Ln-Mg bond length ( $d_1$  and  $d_2$ , Å), displacement of O atom from MgO layer ( $\Delta h$ , Å), angles from  $z$  axis to Mg ( $\theta_{\text{Mg}}$ ) and adsorption energy of Ln adatom ( $E_a$ , eV). The magnetic ground state and TZFS (MAE, meV) of Ln adatoms under three method calculations.

System	$d_1$	$d_2$	$\Delta h$	$\theta_{\text{Mg}}$	$E_a$	$\langle J_z \rangle = \langle L_z \rangle - \langle S_z \rangle$	MAE
Ce (DFT)	2.11	3.50	0.73	143.00°	4.26	0.29 = 0.79 - 0.50	4.15
multiplet						2.50 = 2.86 - 0.36	4.27
Hamiltonian						5/2 = 3 - 1/2	4.17
Nd (DFT)	2.30	3.55	0.66	144.88°	3.44	0.73 = 1.25 - 1.98	10.91
multiplet						0.004 = 0.005 - 0.001	11.22
Hamiltonian						0 = 0 - 0	11.89

state and excited doublets with differing quantum number of  $\Delta m_j = 0, \pm 1$ . When  $C_{4v}$  crystal field symmetry is imposed on the magnetic atom, the indirect QTM between the initial state  $|+J_z\rangle$  and final state  $|-J_z\rangle$  via an intermediate state should satisfied with the following restrictive condition:

$$\Delta m_j = \pm 4m, \pm 4m + 1, \pm 4m - 1 \quad (m = 1, 2, 3, 4) \quad (8)$$

where  $m$  is an integer varying between 0 and  $2J/4$ . For the system with an integer  $J$ , as already stated by Eq. (5), the transitions between initial and final states take place only for  $\Delta m_j = \pm 2, \pm 4, \pm 6$ , and  $\pm 8$ . For the system with a half-integer  $J$  systems, the transitions between any  $|J_z\rangle$  states are allowed.

### III. RESULTS

#### A. Ce adatom on MgO/Ag(100)

##### 1. DFT calculations

Our structural optimizations show that Ce atom exactly stays on O atom instead of Mg atom, as illustrated in Fig. 1. This preferred adsorption site was commonly reported in the late Ln (Gd, Dy, Ho) and TM adatoms on MgO/Ag(100) systems [5,10,26–28,53]. The strong bonding interactions between O and Ce atoms lead to short Ce-O bond length of  $d_1 = 2.11$  Å and tiny displacement of  $\Delta h = 0.73$  Å of O atom toward Ce adatom (Table I). Our adsorption energy  $E_a = 4.26$  eV of Ce atom is significantly larger than 0.93 eV and 0.50 eV of Cu and Ag atoms on the same substrate, respectively [31]. Thus, Ce atom can be stably deposited on MgO layer, indicative of the feasibility of experimental synthesization under the suitable experimental conditions.

To illustrate the bonding characters of Ce adatom, we concerned the deformation charge densities  $\rho$  and orbital-projected density of states (PDOS). From the Figs. 2(a) and 2(b), we can see that charge density shape is nearly axisymmetric, where four accumulation lobes (yellow) are symmetrically surrounded Ce atom and one depletion density (red) is elongated toward O atom. The former seems to be the Ce- $d_{xy}$  orbital shape but the latter is Ce- $d_{z^2}$  orbital shape. From the Figs. 2(c) and 2(d), the morphology of spin density on Ce adatom is analogous with that of charge density of Ce- $d_{xy}$  orbital, beside eight small lobes of Ce- $f_{xyz}$  orbital. These findings indicate some preserved Ce- $d$  electrons, a portion of which participates in bonding interactions with O atom and others are unpaired to show magnetic moment. In combination with the PDOS of Ce atom and its contacting O atom, as

shown in Fig. 3, the remarkable hybridization between Ce- $d_{z^2}$  and O- $p_z$  orbital together with weak hybridization between Ce- $d_{xz/yz}$  and O- $p_x/p_y$  orbitals in the energy range  $-7$  eV to  $-4$  eV verify the yielding of covalent Ce-O bond; spin-polarized Ce- $d_{z^2}$  and Ce- $d_{xy}$  orbitals around the Fermi ( $E_f$ ) level indeed contribute to small magnetic moment.

By analyzing the Mulliken charge population, from Table II, we found that the number of Ce- $4f$  electrons is basically unchanged while Ce- $5d/6s$  orbitals gain/loss  $-0.61/1.29$  electrons compared with freestanding atom. The Ce intra-atomic transfers render 1.61  $|e|$  in Ce- $5d$  orbitals to form the covalent Ce-O bonding; Ce-O interatomic transfers make O atom gets additional  $-0.74 |e|$  to form the ionic Ce-O bonding. Previously, Nd adatom was found to have lost 1.31  $|e|$   $6s$  electrons on graphene [87], and Gd adatom gains 0.54  $|e|$   $5d$  electrons on MgO/Ag(100) [53]. With the method of Bader populations analyses, from the Table S4 within the Supplemental Material [88], charge values lost by Ce and

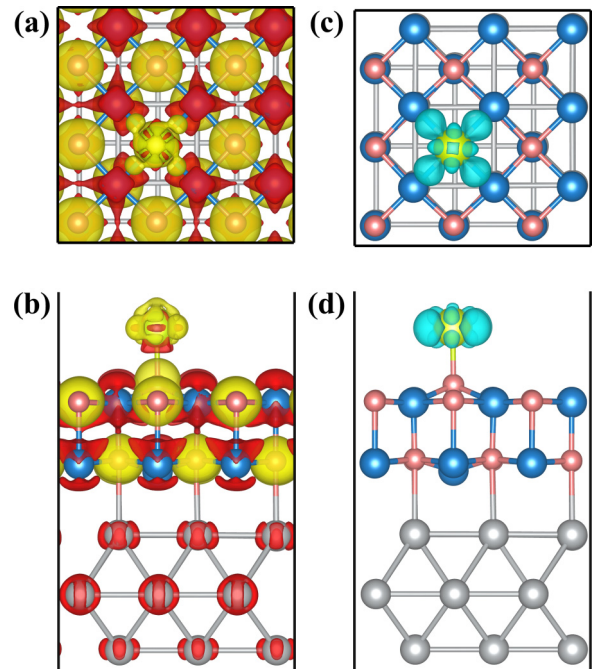


FIG. 2. [(a),(b)] Deformation charge densities with isosurface value  $0.01 \text{ e}/\text{\AA}^3$  for Ce@MgO/Ag(100). Yellow and red colors denote the charge accumulation and depletion, respectively. [(c),(d)] Spin density of Ce@MgO/Ag(100) with isosurface value  $0.008 \text{ e}/\text{\AA}^3$ .

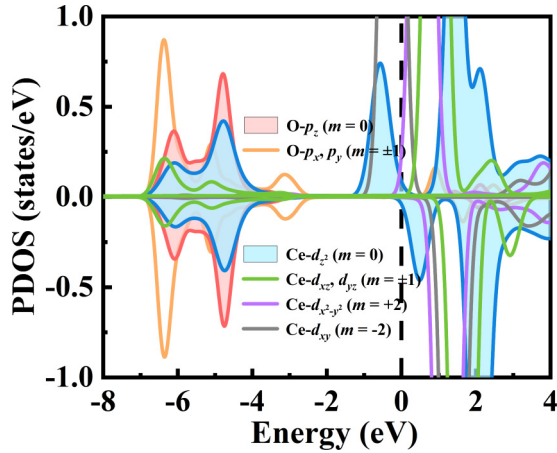


FIG. 3. PDOS of Ce-5d orbitals and O-2p orbitals. The values of Ce-5d orbitals are magnified by 4 times for comparisons.

Mg atoms are close to that given by the Mulliken analyses, but there is a significant difference between two methods for the charge values gained by O atom. This is related to high degree of sensitivity to the atomic basis set and the integration over atomic spheres. We emphasize that the appearance of 5d magnetic moment provides a certain advantage for experimental accessing and controlling of 4f magnetic states using spin-dependent transport techniques. The manipulation of 4f magnetic state can be enabled by the mediated magnetic moment of external 5d shell, which is magnetically coupled with the valence electrons of sensed magnetic atom (interatomic exchange) and the 4f magnetic moment of Ce atom itself (intra-atomic exchange) [58].

The spin and orbital magnetic moments of Ce-4f electrons were calculated by DFT with the GGA+U+vdW+SOC method, and the detailed values were listed in Table I. The obtained  $\mu_S^{4f} = 1.00 \mu_B$  of Ce adatom is essentially identical to the atomic-like value, while  $\mu_L^{4f} = 0.79 \mu_B$  and resultant  $\langle J_z \rangle = 0.29$  are significantly lower than the ideal values of  $3 \mu_B$  and  $\langle J_z \rangle = \pm 5/2$ , respectively. The underestimations of orbital magnetic moment and thus lower  $\langle J_z \rangle$  value are a consequence of intrinsic faultiness of DFT+SOC method in treating the SOC effect as a relativistic perturbation, which can be improved by introducing the orbital polarization effect [89]. Nevertheless, we still propose  $|J_z = \pm 5/2\rangle$  as the ground state by analyzing the angular dependence of 4f charge density in different  $J_z$  magnetic states, i.e., the oblate density for the  $|J_z = \pm 5/2\rangle$  state vs the prolate density for the  $|J_z = \pm 5/2\rangle$

TABLE II. The charge transfer among different orbitals obtained by the Mulliken population analysis (in unit of  $|e|$ ). Negative/positive value denotes gaining/losing electrons.

	Orbital	Ce system	Nd system
Ln adatom	4f	0.00	0.00
	5d	-0.61	-0.44
	6s	+1.29	+1.17
O atom	2p	-0.74	-0.78
Mg atom	3s	+1.80	+1.80

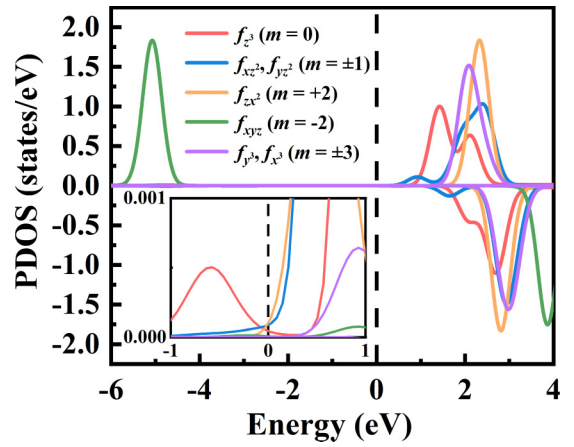


FIG. 4. PDOS of Ce-4f orbitals. Inset chart is amplified PDOS around the Fermi level ( $E_f$ ) in small energy window.

state [90]. To minimize the electrostatic interaction between Ce and O atoms, the ligand field of the underlying MgO substrate will induce an oblate charge density shape of the Ce-4 $f_{xyz}$  state shown in Figs. 2(c) and 2(d), which leads to  $|J_z = \pm 5/2\rangle$  ground state and the out-of-plane MAE. Note that the spin density of Ce-4 $f_{xyz}$  orbital can be deemed as the charge density because its occupied electrons are fully polarized.

Our DFT gives the MAE =  $E_{[100]} - E_{[001]} = 4.15$  meV, which is defined as the total energy difference between [100] and [001] magnetizations. Since the MAE is determined by the electron hopping between the occupied and unoccupied states around the Fermi level ( $E_f$ ) via the SOC effect, we can analyze the PDOS of 4f states based on the second-order perturbation theory [91]. The formula of the matrix contributions can be expressed as

$$\text{MAE} = (\xi)^2 \sum_{o,u} \frac{|\langle o | \hat{L}_z | u \rangle|^2 - |\langle o | \hat{L}_x, \hat{L}_y | u \rangle|^2}{E_u - E_o} \quad (9)$$

where  $\xi$  is the SOC strength,  $\hat{L}_i$  ( $i = x, y, z$ ) is the angular momentum operator, o and u are the occupied and unoccupied electronic states,  $E_o$  and  $E_u$  are energy levels of the occupied and unoccupied 4f states, respectively. If the hopping occurs between the states in the same spin channels ( $ou = \uparrow\uparrow$  or  $\downarrow\downarrow$ ) but with the same/different magnetic quantum number  $m$  ( $|\Delta m| = 0/1$ ) by the operator of  $\hat{L}_z/\hat{L}_{x,y}$ , it gives the positive/negative contributions to out-of-plane MAE; on the contrary, it gives the opposite contributions for the hopping of the occupied and unoccupied states in different spin channels ( $ou = \uparrow\downarrow$  or  $\downarrow\uparrow$ ). From Fig. 4, 4f orbitals of Ce adatom are splitted into five groups:  $f_z^3$  ( $f_0$ ),  $f_{x^2}/f_{y^2}$  ( $f_{\pm 1}$ ),  $f_{xz^2}$  ( $f_{+2}$ ),  $f_{xyz}$  ( $f_{-2}$ ), and  $f_{x^3}/f_{y^3}$  ( $f_{\pm 3}$ ) owing to  $C_{4v}$  symmetry. Since there is basically no occupied spin-down 4f state, the hoppings between  $\downarrow\downarrow$ ,  $\uparrow\downarrow$ , and  $\uparrow\uparrow$  channels can be neglected. Furthermore, the peak of Ce-4 $f_{xyz}$  state is far from the  $E_f$  within an energy difference about 5 eV, indicating that it's contribution to MAE can be ignored. Upon the close inspection of PDOS around the  $E_f$  (inset chart), positive contributions are primarily determined by the matrix elements  $\langle m = \pm 1 \uparrow | \hat{L}_z | m = \pm 1 \uparrow \rangle$ . Although there are



some negative contributions via  $\langle m = 0 \uparrow | \hat{L}_x, \hat{L}_y | m = \pm 1 \uparrow \rangle$  matrices, they are relatively small regarding the large energy difference  $E_u - E_o$  between them. The positive contributions are partially offset by the negative ones, resulting in small net out-of-plane MAE.

## 2. Multiplet simulations

To provide a direct access to the energy spectrum and occupation of Ce quantum states for comparison with the future experiments, we have performed atomic multiplet simulations of the experimentally acquired energy level splitting, XAS and XMCD spectra using the MultiX code [75]. As the MultiX code uses the effective point charge approach for the description of the crystal field generated by the interaction of Ce adatom with the surrounding Mg and O atoms and it can not treat the  $4f$ - $5d$  orbital interactions for the Slater integrals of Hamiltonian, here, we used a pure  $4f$  configuration instead of a  $4f$ - $5d$  mixing configuration in the multiplet simulation. Specifically, if the  $5d$  orbitals are significantly occupied and strongly polarized, the mixing configuration may lead to certain alternations of the quantum levels, XAS and XMCD spectra with respect to the ideal ones that are contributed by all individual electron shells. By matching the experimental XMCD signals with the simulated multiplet spectra using both  $4f^n 5d^0$  and  $4f^n 5d^1$  configurations of Ln adatoms, Singha *et al.* [53] have identified no evidence of unpaired  $5d$  electrons of Ln adatoms on MgO/Ag(100) surface, and they established a charge transfer mechanism leading to an unconventional ionized configuration of Gd( $4f^7 5d^0$ ) and Ho( $4f^{10} 5d^0$ ). Such evidences have been quite commonly observed to occur for Ln adatom on ultrathin MgO and graphene layers on metal surface [58,92]. Although our DFT for Ce adatom on MgO/Ag(100) gives a residual charge about 1.6 electrons in the  $5d$  orbitals using the Mulliken population analyses, which is larger than the DFT values of Gd and Ho adatoms [53], this value is mostly a result of the hybridization between Ce and MgO states. Note that Singha *et al.* [53] have performed the charge analyses with the Löwdin scheme and Donati *et al.* [10] have reported that this method give significantly smaller charge intensities than other methods for Dy atom on MgO/Ag(100). Hence, our multiplet simulation with an assumption of pure  $4f$  configuration may give the reasonable results.

The planar representation is sketched in Fig. 5(a), and the atomic position and strength of charges are listed in the Table III. Our simulated XAS and XMCD spectra in Fig. 6 are characterized by the distinct peaks at 866 eV ( $M_5$ ) and 885 eV ( $M_4$ ), respectively. Both  $M_5$  and  $M_4$  peaks show a fine multiplet structure with a narrow peak, whose intensities are determined by the interactions between the open  $4f$  and  $3d$  shells at the excited state [93,94]. In the XMCD spectra, the maximum intensity is proportional to the projection of total magnetic moment along the beam axis. Thus, higher intensity in normal with respect to grazing incidence of x rays indicates an out-of-plane easy magnetization of this system [5,7,63]. We find no significant difference in the simulated XAS line shape of Ce adatom in comparison with that of the freestanding Ce atom [9,93–95]. It reveals the Ce in the  $f^1$  configuration. As a result, the lowest multiplet of Ce adatom

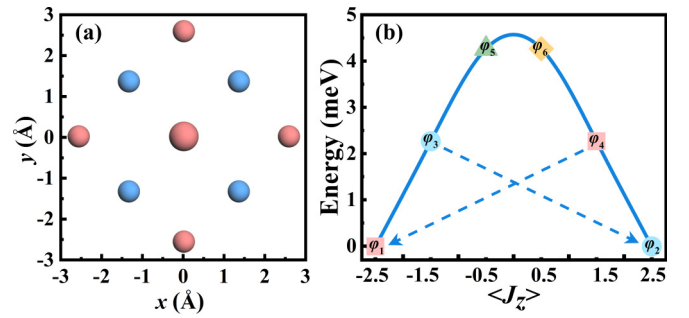


FIG. 5. (a) Planar representation of the charge CF scheme. Pink and blue marks positive and blue negative charge, respectively, and size of each circle reflects the amount of charge. (b) Energy levels with the eigenstates as a function of the expectation value  $\langle J_z \rangle$  in multiplet simulations for Ce adatom on MgO/Ag(100).

is characterized by  $S = 1/2$ ,  $L = 3$ ,  $J = 5/2$ , and multiplicity of  $2J + 1 = 6$ . Figure 5(b) illustrates the simulated energy level distribution of Ce adatom in the lowest  $J = 5/2$  multiplet, indicating the doublet ground states of  $\langle J_z \rangle = \pm 5/2$  with  $\langle S_z \rangle = 0.36$  and  $\langle L_z \rangle = 2.86$ . The simulated out-of-plane  $\text{MAE}_{\text{Mult}} = 4.27$  meV is in good agreement with DFT calculation  $\text{MAE}_{\text{DFT}} = 4.15$  meV. As listed in the Table S5 within the Supplemental Material [88], we found that the doublet ground states are separated by 2.27 meV and 4.27 meV from the  $\langle J_z \rangle = \pm 3/2$  and  $\langle J_z \rangle = \pm 1/2$  excited states, respectively, giving the  $U_{\text{rev}} = 2.27$  meV for the spin-flip excitation. In Fig. 6(b), the XMCD amplitude is large at normal incidence ( $\theta = 0^\circ$ ) compared to grazing incidence, which is the fingerprint of Ce adatom with an out-of-plane easy axis and large MAE.

## 3. CF Hamiltonian calculations

Since Ce adatom is exactly localized at  $C_{4v}$  symmetric site on MgO/Ag(100) substrate and its  $5d6s$  electrons dominantly participate in the bonding interactions, the CF Hamiltonian (2) can be simplified as the dominant (quadratic) uniaxial term [65,84],

$$H = |D|J_z^2 \quad (10)$$

where  $D$  denotes the lowest-order uniaxial anisotropy constant and  $J_z$  is the  $z$  axis component of total angular momentum  $J$ . As the uniaxial operators  $O_n^0$  in the spin Hamiltonian equa-

TABLE III. The atomic positions and charges in multiplet simulations for Ce@MgO/Ag(100) system.

Element	$x$ (Å)	$y$ (Å)	$z$ (Å)	Charge (e)
O	0.00	0.00	-2.11	-0.0145
O	1.50	-1.48	-2.81	0.010
O	-1.50	-1.48	-2.81	0.010
O	-1.50	1.48	-2.81	0.010
O	1.50	1.48	-2.81	0.010
Mg	0.00	-2.85	-2.69	-0.010
Mg	2.85	0.00	-2.69	-0.010
Mg	-2.85	-2.85	-2.69	-0.010
Mg	0.00	2.85	-2.69	-0.010

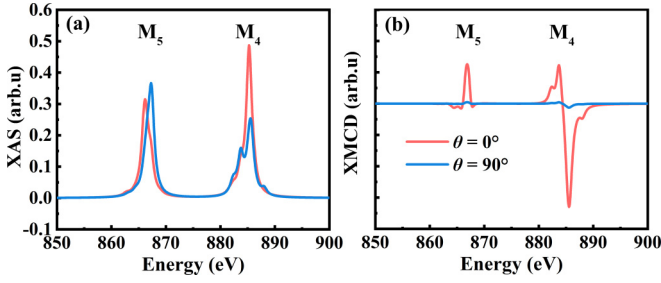


FIG. 6. Simulated (a) XAS and (b) XMCD spectra of Ce@MgO/Ag(100). Red and blue represents normal ( $\theta = 0^\circ$ ) and grazing ( $\theta = 90^\circ$ ) incidence spectra, respectively.

tion (2) commute with the  $z$ -projected total moment operator  $\hat{J}_z$  and give the main contribution to the splitting along the out-of-plane direction,  $|D|$  values would determine the TZFS of the magnetic states. Mapping our DFT obtained MAE(TZFS) = 4.15 meV and proposed angular momentum  $\langle J_z \rangle = \pm 5/2$  of the ground states to this Hamiltonian, we derived the uniaxial anisotropy constant of  $|D| = 0.66$  meV. This value is very close to  $|D| = 0.75 \pm 0.03$  meV and  $|D| = 0.86 \pm 0.03$  meV for Gd atom on Cu(111) and Pt(111) surfaces through the fittings of the single spin inelastic electron tunneling spectroscopy (IETS) spectra [47]. Since  $D < 0$  and  $D > 0$  indicate the easy axis perpendicular to the surface plane and in the surface plane, respectively,  $D = -0.66$  meV is the actual value because of out-of-plane MAE of DFT calculations. In terms of  $D=3B_2^0$  proposed by Kozanecki *et al.* [23], we estimated the CF parameter  $B_2^0 = -221$   $\mu\text{eV}$  for Ce adatom. Using the obtained uniaxial anisotropy  $|D|$ , we can also estimate  $U_{\text{rev}}$  (spin-flip energy  $E_{sf}$ ) for the spin-flip excitation between the ground states with  $J_z = \pm J$  and the first excited states with  $J_z = \pm(J-1)$  via  $E_{sf} = |D|((J-1)^2 - J^2) = D(2J-1)$ . According to  $J = 5/2$  and  $|D| = 0.66$  meV, we obtained  $U_{\text{rev}} = E_{sf} = 2.64$  meV, which is very close to 2.27 meV of the multiplet simulation.

Next, we would like to accurately rationalize the quantum levels, MAE and  $U_{\text{rev}}$  for Ce adatom on MgO/Ag(100) via solving the CF model Hamiltonian of Ce adatom. For the  $4f^1$  configuration, the lowest  $J$  multiplet is the  ${}^2F_{5/2}$  term characterized by  $L = 3$ ,  $S = 1/2$ ,  $J = 5/2$ , and multiplicity of  $2J + 1 = 6$ . According to Eq. (2),  $B_6^0 O_6^0$  and  $B_6^4 O_6^4$  terms vanish because of  $n \leq 2J = 5$ . The Hamiltonian for this system can be written as

$$H_{4v}^{\text{Ce}} = B_2^0 O_2^0 + B_4^0 O_4^0 + B_4^4 O_4^4. \quad (11)$$

We defined the [001] crystallographic direction as the quantization axis  $z$  and the [100] direction as the  $x$  axis. Adopting six  $J_z$  states  $|m_j\rangle = |\pm 5/2\rangle, |\pm 3/2\rangle, |\pm 1/2\rangle$  as the basis set,  $H_{4v}^{\text{Ce}}$  Hamiltonian can be expressed as a (6 $\times$ 6) matrix listed as Table IV, and the nonzero matrix elements will be calculated. The parameters A, B, C, D can be given as

$$\begin{aligned} A &= 10B_2^0 + 60B_4^0, \\ B &= -2B_2^0 - 180B_4^0, \\ C &= -8B_2^0 + 120B_4^0, \\ D &= 12\sqrt{5}B_4^0. \end{aligned} \quad (12)$$

TABLE IV.  $H_{4v}^{\text{Ce}}$  Hamiltonian matrix.

$ J_z = m_j\rangle$	$ -5/2\rangle$	$ -3/2\rangle$	$ -1/2\rangle$	$ +1/2\rangle$	$ +3/2\rangle$	$ +5/2\rangle$
$\langle -5/2 $	A	0	0	0	D	0
$\langle -3/2 $	0	B	0	0	0	D
$\langle -1/2 $	0	0	C	0	0	0
$\langle +1/2 $	0	0	0	C	0	0
$\langle +3/2 $	D	0	0	0	B	0
$\langle +5/2 $	0	D	0	0	0	A

By solving above Hamiltonian equation, in principle, we can get six eigenstates  $\psi_m^\lambda$  ( $m = \frac{1}{2} - \frac{5}{2}$ ;  $\lambda = +, -$ ) and six eigenvalues  $\varepsilon_{m^\pm}$ , respectively. For simplicity, we give six eigenstates in an universal expression, each of which is the combinations of two  $J_z$  states with a quantum number differing by  $\Delta m_j = 4$  due to the fourfold symmetry of ligand field that Ce adatom suffers. The  $\psi_{\frac{1}{2}}^\pm$  states are the pure  $J_z$  states because of the maximum/minimum angular momentum  $J_z = \pm \frac{5}{2}$ ,

$$\begin{aligned} \varepsilon_{\frac{5}{2}^\pm} &= \frac{A+B}{2} + \sqrt{\left(\frac{A-B}{2}\right)^2 + D^2}, \\ \varepsilon_{\frac{3}{2}^\pm} &= \frac{A+B}{2} - \sqrt{\left(\frac{A-B}{2}\right)^2 + D^2}, \end{aligned} \quad (13)$$

$$\varepsilon_{\frac{1}{2}^\pm} = -8(B_2^0 - 15B_4^0),$$

$$\begin{aligned} \psi_{\frac{5}{2}}^+ &= \sum_{w=0}^1 c_{\frac{5}{2},w}^+ \left| \frac{5}{2} - 4w \right\rangle = c_{\frac{5}{2},0}^+ \left| \frac{5}{2} \right\rangle + c_{\frac{5}{2},1}^+ \left| -\frac{3}{2} \right\rangle, \\ \psi_{\frac{3}{2}}^- &= \sum_{w=0}^1 c_{\frac{3}{2},w}^- \left| -\frac{5}{2} + 4w \right\rangle = c_{\frac{3}{2},0}^- \left| -\frac{5}{2} \right\rangle + c_{\frac{3}{2},1}^- \left| \frac{3}{2} \right\rangle, \\ \psi_{\frac{3}{2}}^+ &= \sum_{w=0}^1 c_{\frac{3}{2},w}^+ \left| \frac{3}{2} - 4w \right\rangle = c_{\frac{3}{2},0}^+ \left| \frac{3}{2} \right\rangle + c_{\frac{3}{2},1}^+ \left| -\frac{5}{2} \right\rangle, \\ \psi_{\frac{1}{2}}^- &= \sum_{w=0}^1 c_{\frac{1}{2},w}^- \left| -\frac{3}{2} + 4w \right\rangle = c_{\frac{1}{2},0}^- \left| -\frac{3}{2} \right\rangle + c_{\frac{1}{2},1}^- \left| \frac{5}{2} \right\rangle, \\ \psi_{\frac{1}{2}}^+ &= \sum_{w=0}^0 c_{\frac{1}{2},w}^+ \left| \frac{1}{2} - 4w \right\rangle = c_{\frac{1}{2},0}^+ \left| \frac{1}{2} \right\rangle, \\ \psi_{\frac{1}{2}}^- &= \sum_{w=0}^0 c_{\frac{1}{2},w}^- \left| -\frac{1}{2} + 4w \right\rangle = c_{\frac{1}{2},0}^- \left| -\frac{1}{2} \right\rangle. \end{aligned} \quad (14)$$

To get the numerical solutions of eigenstates and eigenvalues, firstly, the CF parameters  $B_n^k$  should be determined. Conventionally, these parameters are quite often determined by matching the energy splitting measured in spin excitation spectra with the CF modeling calculations. By fitting the energy thresholds for magnetization switching in spin Hamiltonian calculations with STM experiments, Natterer *et al.* [51] have determined  $B_2^0 = -835$   $\mu\text{eV}$ ,  $B_4^0 = -100$  neV,  $B_6^0 = 8.6$  neV,  $B_4^4 = 3.7$   $\mu\text{eV}$ , and  $B_6^4 = 0$  neV for Ho adatom on MgO(100), and Donati *et al.* [96] have proposed



$B_2^0 = -140 \sim 96 \mu\text{eV}$  and  $B_4^0 = -0.85 \sim 1.06 \mu\text{eV}$  for Ho and Er adatoms on Cu/Pt(111); Baltic *et al.* [9] have given  $B_2^0$  on the order of hundred  $\mu\text{eV}$  and  $B_4^0$  on the order of several hundred neV for Ln (Ln = Nd, Tb, Dy, Ho, Er) adatoms on the graphene/Ir(111) by comparing the measured ISTS spectra and the energy diagram of magnetic states with the multiplet calculations. On the other hand,  $B_n^k$  can be calculated from the point charge electrostatic model starting from the interaction energy of the  $4f$  electrons with all other ligand charges [97]. In this regard, Miyamachi *et al.* [4] have theoretically given the CF parameters of  $B_2^0 = -239 \mu\text{eV}$  and  $B_4^0 = 86 \text{ neV}$  for Ho atom on Pt(111) surface. Since the CF Hamiltonian can be expressed in terms of different representations: spherical harmonics and Stevens operators, different notational conventions of the CF Hamiltonian are related to each other by equivalence coefficients, i.e., the CF parameters  $B_n^k$  can be calculated by the following expression (Eqs. S1–S10 within the Supplemental Material [88]):

$$B_n^k = -\frac{q_M}{4\pi\epsilon_0} \frac{\gamma_{nk} \langle r^n \rangle \langle W_n^k \rangle}{\langle O_n^k \rangle} \quad (15)$$

where  $q_M$  denotes the total charges of magnetic Ln atom,  $\gamma_{nk} = \sum_{j=1}^J \frac{4\pi}{(2n+1)} \frac{(-1)^k Y_n^{-k}(\theta_j, \phi_j)}{R_j^{n+1}} q_{O/Mg}$  is the numerical factor that relates with the spherical harmonics and total charges of O and Mg atoms of the nearest neighbor of Ln adatom,  $\langle W_n^k \rangle = \int_0^{2\pi} \int_0^\pi Y_l^{m*}(\theta_i, \phi_i) Y_n^k(\theta_i, \phi_i) Y_l^m(\theta_i, \phi_i) \sin(\theta_i) d\theta_i d\phi_i$  is the matrix element of the electron angular part for the  $4f$  wave function,  $\langle r^n \rangle = \int_0^\infty R_{n_i}(r_i)^2 r_i^n r_i^2 dr_i$  is the expectation value of the electron radial part for the  $4f$  wave function, and  $\langle O_n^k \rangle$  is the expectation value of the CF Hamiltonian in the form of Stevens operators.

With the atomic charges and structural parameters extracted from our DFT calculations, as listed in Tables I and II, we can calculate numerical values of  $\gamma_{nk}$ . Furthermore,  $\langle O_n^k \rangle$  and  $\langle W_n^k \rangle$  can be obtained regarding the ground state of  $\langle J = 5/2, J_z = -5/2 \rangle$  of Ce adatom, and  $\langle r^n \rangle$  can be roughly derived from the references for the Ln ions in bulk or gas phases [98]. As a consequence, we derived  $B_2^0 = -227 \mu\text{eV}$ ,  $B_4^0 = 83 \mu\text{eV}$ , and  $B_4^4 = -18 \mu\text{eV}$  (Table S6) as discussed in the section of crystal parameters in the Supplemental Material [88]. However, we should emphasize that our obtained Mulliken charges and adopted radial integrals  $\langle r^n \rangle$  are only taken as more realistic estimations: (i) the local charge is not well defined on the extended surface systems, and it sensitively depends on the calculated methods like the Bader and Mulliken analyses that give the distinguishable values for Ce adatom (Table S4 within the Supplemental Material [88]) and (ii)  $\langle r^n \rangle$  of Ce adatom will not coincide with the ionic limit and they could be significantly different from those of the bulk and gas phase ions. Although the point charge electrostatic model has well-known limitation to accurately calculate the CF parameters  $B_n^k$  because of unoptimal  $\langle r^n \rangle$  and charge distributions [99], it still provides a way to give the theoretical approximations. Typically, the CF parameter  $B_2^0 = -227 \mu\text{eV}$  we obtained by using the point charge electrostatic model is not only very close to  $B_2^0 = -221 \mu\text{eV}$  obtained by using the simplified CF Hamiltonian, but also approaches to these reported values for Ln atoms on surfaces [4,9]. However,

TABLE V. Eigenvalues and eigenvectors as well as the expectation  $\langle J_z \rangle$  of different magnetic states calculated from the CF model Hamiltonian  $H_{4v}^{\text{Ce}}$  equation for Ce@MgO/Ag(100) system.

Eigenstate	Eigenvalue (meV)	$\langle J_z \rangle$	Eigenvectors
$\varphi_1(\psi_{-\frac{5}{2}})$	-2.35	-5/2	$ -5/2\rangle$
$\varphi_2(\psi_{+\frac{5}{2}})$	-2.35	+5/2	$ +5/2\rangle$
$\varphi_3(\psi_{-\frac{3}{2}})$	0.52	-3/2	$ -3/2\rangle$
$\varphi_4(\psi_{+\frac{3}{2}})$	0.52	+3/2	$ +3/2\rangle$
$\varphi_5(\psi_{-\frac{1}{2}})$	1.82	-1/2	$ -1/2\rangle$
$\varphi_6(\psi_{+\frac{1}{2}})$	1.82	+1/2	$ +1/2\rangle$

the energy spectrum obtained by feeding all parameters into Hamiltonian calculations (Table S7 within the Supplemental Material [88]) differs greatly from the multiplet simulated energy spectrum shown in Fig. 5(b). By examining the contributions of  $B_2^0$ ,  $B_4^0$ , and  $B_4^4$  to the energy spectrum, we found that  $B_2^0$  contribution can basically reproduce the simulated energy spectrum and  $B_4^4$  contribution is very small, while  $B_4^0$  contribution makes a significantly change of the energy spectrum. Regarding the values of  $B_2^0$  of Ln adatom on the order of hundred neV [4,9,51],  $B_4^0 = 83 \text{ neV}$  was actually employed in the calculations.

After getting the CF parameters, we can calculate the numerical eigenvalues and analytical eigenstates of  $H_{4v}^{\text{Ce}}$  Hamiltonian. From the Table V, we found that these eigenstates are almost pure  $J_z$  states, where  $\psi_{\frac{5}{2}}^{\pm} = |m_j = \pm \frac{5}{2}\rangle$ ,  $\psi_{\frac{3}{2}}^{\pm} = |m_j = \pm \frac{3}{2}\rangle$ , and  $\psi_{\frac{1}{2}}^{\pm} = |m_j = \pm \frac{1}{2}\rangle$  are labeled as  $\varphi_{1,2}$ ,  $\varphi_{3,4}$ , and  $\varphi_{5,6}$ , respectively. These nonmixed states are traced to near zero matrix elements contributed by the transverse  $B_4^4 O_4^4$  term. Correspondingly, the resultant eigenvalues are  $\varepsilon_{5/2}^{\pm} = \varepsilon_{1,2} = -2.35 \text{ meV}$ ,  $\varepsilon_{3/2}^{\pm} = \varepsilon_{3,4} = 0.52 \text{ meV}$ ,  $\varepsilon_{1/2}^{\pm} = \varepsilon_{5,6} = 1.82 \text{ meV}$ , respectively. In Fig. 7(a), we plotted the energy spectrum for Ce adatom and we can see that six eigenstates are splitted into three doublet states owing to the CF interaction. The CF model Hamiltonian  $\text{MAE}_{\text{CF}} = 4.17 \text{ meV}$  is consistent with the DFT calculated  $\text{MAE}_{\text{DFT}} = 4.15 \text{ meV}$  and

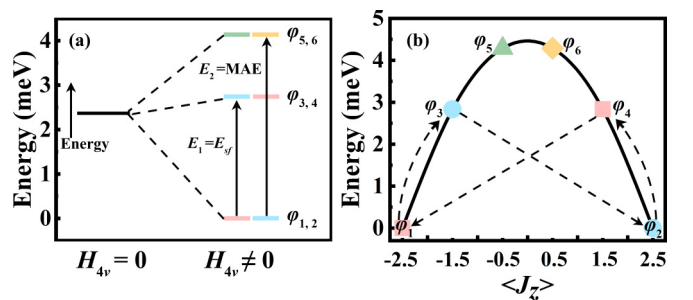


FIG. 7. (a) Energy diagram of Ce atom on MgO/Ag(111). (b) Energy levels as a function of the expectation value  $\langle J_z \rangle$  with the CF model Hamiltonian  $H_{4v}^{\text{Ce}}$  calculation. The parabola line indicates the anisotropy barrier. The relaxation mechanism for magnetization reversal are illustrated by arrows via the spin-flipped excitation from  $J_z = \mp 5/2$  to  $J_z = \mp 3/2$  doublet, namely, from left to right electron-induced switching or ladder transitions over the effective barrier.

the multiplet simulated  $MAE_{\text{Mult}} = 4.27$  meV. The first excited energy  $E_{sf} = 2.87$  meV from the CF Hamiltonian calculation is approach to 2.64 meV and 2.27 meV from simplified Hamiltonian and multiplet simulation, respectively.

Inspection of  $J_z$  components of six eigenstates in Eq. (14), these eigenstates are classified into four classes with respect to the same mixture of  $J_z$  states:  $\{\varphi_1, \varphi_4\}$ ,  $\{\varphi_2, \varphi_3\}$ ,  $\varphi_5$ , and  $\varphi_6$ , which are marked by pink, azure, green, and yellow colors in the energy level diagram of Fig. 7(b), respectively. We found the down-turned parabola with the doublet ground states of  $|J = \frac{5}{2}, m_j = \pm \frac{5}{2}\rangle$  in pink and azure colors, respectively. Since two degenerate ground states that possess the angular moments pointing into or out of the surface are belong to different classes, the direct QTM between them is prohibited owing to  $\langle \frac{5}{2}^{\pm} | J_z | \frac{5}{2}^{\mp} \rangle = 0$  and  $\langle \frac{5}{2}^{\pm} | (J_-^4, J_+^4) | \frac{5}{2}^{\mp} \rangle = 0$ . This is consistent with the Kramers theorem for the magnetic ion with half-integer  $J$  [9]. However, the scattering by thermally activated energy of 2.87 meV enables the spin-flip events from the ground states  $|J_z = \pm \frac{5}{2}\rangle$  to the lowest-lying excited states  $|J_z = \pm \frac{3}{2}\rangle$ . As each eigenstate of two lowest-lying excited eigenstates becomes accessible to mix with the ground state via the nonzero matrix elements  $\langle \frac{3}{2}^{\pm} | (J_-^4, J_+^4) | \frac{5}{2}^{\mp} \rangle \neq 0$ , i.e.,  $\Delta m_j = \pm 4$  is an integer multiple of 4, it opens the thermally activated magnetization relaxation channels via the underbarrier spin-flip transitions accessible with tunneling electron. On the whole, the reversal paths involve the spin-flipped excitations from the ground doublet  $|\pm \frac{5}{2}\rangle$  toward the intermediate states  $|\pm \frac{3}{2}\rangle$  by the single electron scattering, and the relaxation process from  $|\pm \frac{3}{2}\rangle$  states to the final states  $|\mp \frac{5}{2}\rangle$  with opposite orientation of the initial one. The decreasing accessible energy of  $MAE = 4.17$  meV to  $U_{\text{rev}} = 2.87$  meV shortcuts the energy barrier, providing the relatively easy switch from one ground state to the other via the combination of thermal excitation and electron scattering. In addition, the phonon-induced transition is protected by this splitting energy due to the vanished phonon density of states in low energy range 0 – 25 meV of MgO layers [5,16].

To describe the magnetization relaxation of a system at temperature  $T$ , the zero-field magnetic lifetime  $\tau$  can be quantitatively evaluated exponentially with temperature  $T$  following the Arrhenius law:  $\tau = \tau_0 e^{U_{\text{rev}}/k_B T}$ , where  $\tau_0$  is the characteristic time between two consecutive reversal attempts and  $k_B$  is the Boltzmann constant, and spin-flip barrier  $U_{\text{rev}}$  is available in aforementioned calculations. As  $\tau_0$  is primarily dependent on the phonons and scattering electrons of MgO substrate, it can be estimated for Ho adatom on MgO/Ag(100) by using the measured magnetic lifetime of 1586 s at 10 K and  $U_{\text{rev}}$  of 4.5 meV [5]. Taking the derived  $\tau_0 = 8.56$  s and  $U_{\text{rev}} = 2.87$  meV, we calculated the magnetic lifetime Ce atom on MgO to be 239 s at 10 K. This lifetime is long enough for the acquisition of a single point in the magnetization curves, which may give the magnetic hysteresis in future measurements.

## B. Nd adatom on MgO/Ag(100)

### 1. DFT calculations

In the comparison of structural parameters between Ce and Nd adsorptions, from Table I we found that Nd adatom gives

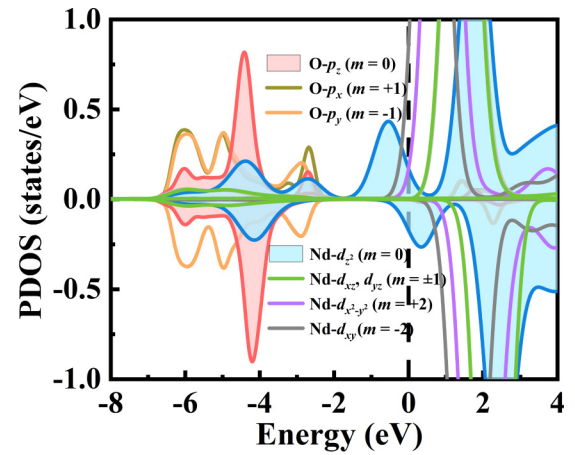


FIG. 8. The PDOS of Nd-5d orbitals and O-2p orbitals. The values of Nd-5d orbitals are magnified by 4 times for comparisons.

the longer Nd-O bond-length  $d_1 = 2.30$  Å and the shorter displacement of underneath O atom  $\Delta h = 0.66$  Å, and thus smaller adsorption energy  $E_a = 3.44$  eV. Although very similar behavior is observed in the PDOS of Ce-5d orbital (Fig. 3) and Nd-5d orbital (Fig. 8), i.e., the hybridization between Ln- $d_{z^2}$  and O- $p_z$  orbitals in the energy range  $-6$  eV to  $-2$  eV as well as the spin-splitting of Ln- $d_{z^2}$  and Ln- $d_{xy}$  orbitals around the  $E_f$ , notwithstanding, the hybridization strength of Nd adatom is relatively lower due to fewer 5d electrons ( $-0.44 |e|$  from the Mulliken charge population in Table II). As a result, the feeble Nd $_{5d}$ -O $_{2p}$  hybridizations lead to the weaker covalent bonding interaction between the Nd adatom and the underneath O atom in Nd@MgO/Ag(111) system. By analyzing the deformation charge densities  $\rho$  shown in Figs. 9(a) and 9(b), charge depletion on the bottom of Nd atom

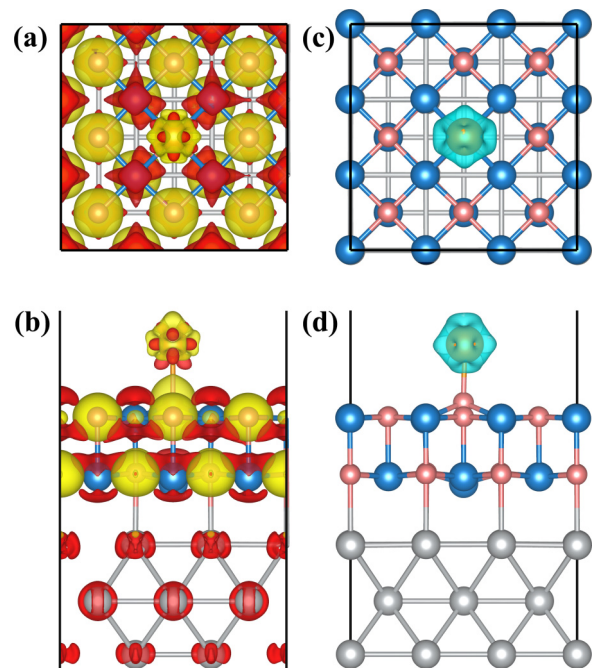


FIG. 9. Same as in Fig. 2 but for Nd adatom.

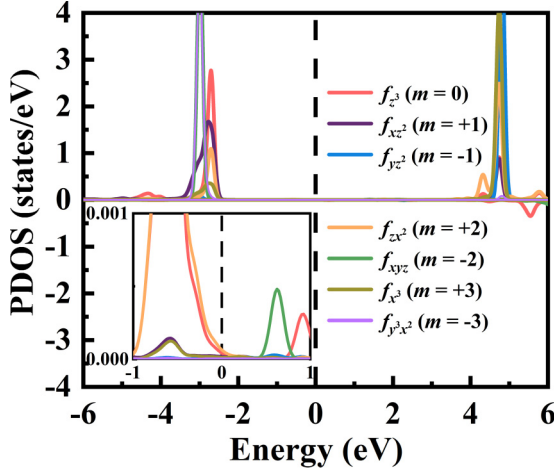


FIG. 10. Same as in Fig. 4 but for Nd-4f orbitals.

(red density) and charge accumulation on the top of O atom (yellow density) validate the formation of Nd-O ionic bond, which is also supported by  $-0.78 |e|$  charge transfers from Nd adatom toward O atom, mostly from the outer 6s shell. Typically, the loss of  $1.17 |e|$  Nd-6s in Nd@MgO/Ag(100) is approach to previous DFT calculations on Ln (Nd, Gd, Eu) adatoms that a half of 6s electrons are lost in Ln@graphene [87]. The adsorption induces a reorganization of the electronic configuration of 5d6s shell yet not 4f shell, with some electrons transferred from the 6s orbitals to the intra-atomic 5d orbital and underneath O atom.

We resolved the magnetism on individual orbital of Nd adatom based on DFT calculations, and found spin magnetic moment  $\mu_S^{5d} = 0.16 \mu_B$ ,  $\mu_S^{6s} = 0.69 \mu_B$ ,  $\mu_S^{4f} = 4\mu_B$  and orbital magnetic moment of  $\mu_L^{4f} = 1.25 \mu_B$ , respectively. The spin density in Figs. 9(c) and 9(d) clearly display a net spin-polarization of the 4f shell (inner density) and 5d shell (outer density). Although orbital moment of Nd-4f electrons is significantly quenched with respect to freestanding atomic-like value of  $6 \mu_B$ , four 4f electrons have the spin-up occupation and consequently  $4f^4$  electronic configuration are still preserved in Nd adatom. Nevertheless, bond formation distorts the atomic-like 4f suborbital occupations that are predicted by the Hund's rule, quenching the orbital angular momentum and orbital magnetic moment [1]. The DFT energy calculations show that Nd system has out-of-plane  $\text{MAE}_{\text{DFT}} = 10.91$  meV. To unravel the mechanism determining the MAE with the filling of Nd-4f orbital, we can analyze the PDOS of Nd-4f orbitals around the  $E_f$  level. From the Fig. 10, the electron hopping between the occupied  $f_{+2}$  state and the unoccupied  $f_{-2}$  states, via the coupling matrix element  $\langle m = +2^\uparrow | \hat{L}_z | m = -2^\uparrow \rangle$ , dominantly contributes to the out-of-plane MAE. Note that the hopping between the occupied  $f_0$  state and unoccupied  $f_{-2}$  states does not occur due to  $|\Delta m| = 2$ .

## 2. Multiplet simulation

Based on the atomic position and strength of charges listed in the Table VI, we simulated XAS spectrum and energy diagram of Nd adatom. Figure 11(a) shows the XAS spectrum

TABLE VI. The atomic positions and charges in multiplet simulations for Nd@MgO/Ag(100) system.

Element	x (Å)	y (Å)	z (Å)	Charge (e)
O	0.00	0.00	-2.11	-0.008
O	1.50	-1.49	-2.80	0.30
O	-1.50	-1.49	-2.80	0.30
O	-1.49	1.50	-2.80	0.30
O	1.49	1.50	-2.80	0.30
Mg	0.00	-2.86	-2.69	-0.30
Mg	2.86	0.00	-2.69	-0.30
Mg	-2.86	-2.86	-2.69	-0.30
Mg	0.00	2.86	-2.69	0.30

of Nd adatom acquired at  $M_5$  (959 eV) and  $M_4$  (981 eV) edges in two circular polarizations ( $\theta=0^\circ, 90^\circ$ ). The XAS line shape of Nd adatom adsorbed on MgO/Ag(100) matches well the experimental one of freestanding Nd atom, verifying the multiplet ground state of Nd adatom in the  $4f^4$  configuration ( $4f^4: L = 6, S = 2, J = 4$ ) [93]. For Nd adatom on the bare graphene monolayer or graphene/Ir(111) substrate, similar occupation with nearly 4 electrons in 4f orbitals has been drawn by comparing the DFT calculation and experimental measurement [9,100]. With the aforementioned electronic configuration, analogously, the multiplet simulation gives three groups of degenerate eigenvalues of 0 meV, 4.44 meV, 10.81 meV and three nondegenerate eigenvalues of 8.91 meV, 9.68 meV, and 11.22 meV, respectively, which are illustrated as the energy diagram in Fig. 11(b) and listed in Table S8 within the Supplemental Material [88]. Consequently, we get the deduced  $\text{MAE}_{\text{Mult}} = 11.22$  meV, which is close to  $\text{MAE}_{\text{DFT}} = 10.91$  meV. From the Table S8 within the Supplemental Material [88], we note that a pair of singlet ground states have the nearly quenched magnetic moment  $\langle J_z \rangle = \langle L_z \rangle + \langle S_z \rangle = \pm 0.004$ . Such tunnel-split doublet separation strongly reduces  $U_{\text{rev}}$  to a nearly zero energy and thus gives the absence of magnetic hysteresis in Nd atoms.

## 3. CF Hamiltonian calculations

For Nd adatom in the  $4f^4$  configuration, its lowest  $J$ -multiplet  $^5I_4$  term is characterized by  $L = 6, S = 2, J = 4$ , and multiplicity of  $2J+1 = 9$ . If we take nine  $J_z$  states  $|m_j = \pm 4, \pm 3, \pm 2, \pm 1, 0\rangle$  as the basis set, the CF model Hamiltonian (16) can be expressed as a  $(9 \times 9)$  matrix (Table VII). By solving Hamiltonian matrix, we got nine eigenstates  $\psi_m^\lambda$  ( $m = 0 - 4; \lambda = +, -, 0$ ) and listed them in Eq. (17). Note

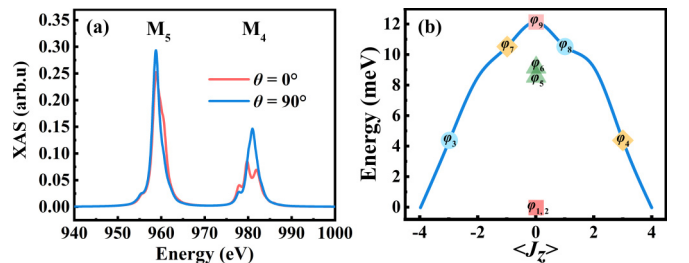


FIG. 11. Simulated XAS spectra (a) and energy levels (b) for Nd@MgO/Ag(100) system.



TABLE VII.  $H_{4v}^{\text{Nd}}$  Hamiltonian matrix.

$ J_z\rangle$	$ -4\rangle$	$ -3\rangle$	$ -2\rangle$	$ -1\rangle$	$ 0\rangle$	$ +1\rangle$	$ +2\rangle$	$ +3\rangle$	$ +4\rangle$
$\langle -4 $	E	0	0	0	J	0	0	0	0
$\langle -3 $	0	F	0	0	0	K	0	0	0
$\langle -2 $	0	0	G	0	0	0	L	0	0
$\langle -1 $	0	0	0	H	0	0	0	K	0
$\langle 0 $	J	0	0	0	I	0	0	0	J
$\langle +1 $	0	K	0	0	0	H	0	0	0
$\langle +2 $	0	0	L	0	0	0	G	0	0
$\langle +3 $	0	0	0	K	0	0	0	F	0
$\langle +4 $	0	0	0	0	J	0	0	0	E

that the parameters E-L in the Hamiltonian matrix were given in the expressions (18),

$$H_{4v}^{\text{Nd}} = B_2^0 O_2^0 + B_4^0 O_4^0 + B_6^0 O_6^0 + B_4^4 O_4^4 + B_6^4 O_6^4, \quad (16)$$

$$\psi_4^+ = \sum_{w=0}^2 c_{4,w}^+ |4-4w\rangle = c_{4,0}^+ |4\rangle + c_{4,1}^+ |0\rangle + c_{4,2}^+ |-4\rangle,$$

$$\psi_4^- = \sum_{w=0}^2 c_{4,w}^- |-4+4w\rangle = c_{4,0}^- |-4\rangle + c_{4,1}^- |0\rangle + c_{4,2}^- |4\rangle,$$

$$\psi_3^+ = \sum_{w=0}^1 c_{3,w}^+ |3-4w\rangle = c_{3,0}^+ |3\rangle + c_{3,1}^+ |-1\rangle,$$

$$\psi_3^- = \sum_{w=0}^1 c_{3,w}^- |-3+4w\rangle = c_{3,0}^- |-3\rangle + c_{3,1}^- |1\rangle,$$

$$\psi_2^+ = \sum_{w=0}^1 c_{2,w}^+ |2-4w\rangle = c_{2,0}^+ |2\rangle + c_{2,1}^+ |-2\rangle,$$

$$\psi_2^- = \sum_{w=0}^1 c_{2,w}^- |-2+4w\rangle = c_{2,0}^- |-2\rangle + c_{2,1}^- |2\rangle,$$

$$\psi_1^+ = \sum_{w=0}^1 c_{1,w}^+ |1-4w\rangle = c_{1,0}^+ |1\rangle + c_{1,1}^+ |-3\rangle,$$

$$\psi_1^- = \sum_{w=0}^1 c_{1,w}^- |-1+4w\rangle = c_{1,0}^- |-1\rangle + c_{1,1}^- |3\rangle,$$

$$\psi_0^0 = \sum_{w=0}^0 c_{0,w} |4w\rangle = c_{0,0} |0\rangle + c_{0,1} |4\rangle, \quad (17)$$

$$E = 28B_2^0 + 840B_4^0 + 5040B_6^0,$$

$$F = 7B_2^0 - 1260B_4^0 - 21420B_6^0,$$

$$G = -8B_2^0 - 660B_4^0 + 27720B_6^0,$$

$$H = -17B_2^0 + 540B_4^0 + 1260B_6^0,$$

$$I = -20B_2^0 + 1080B_4^0 - 25200B_6^0,$$

$$J = 12\sqrt{70}B_4^4 + 360\sqrt{70}B_6^4,$$

$$K = 60\sqrt{7}B_4^4 - 180\sqrt{7}B_6^4, \quad L = 180B_4^4 - 2520B_6^4. \quad (18)$$

TABLE VIII. Eigenvalues (meV) and eigenvectors as well as the expectation  $\langle J_z \rangle$  of different magnetic states calculated from the CF model Hamiltonian for Nd@MgO/Ag(100) system. Eigenvectors are described as a supercomposition of  $J_z$  states belonging to the lowest  $J = 4$  multiplet.

Eigenstate	Eigenvalues	$\langle J_z \rangle$	Eigenvectors
$\varphi_1(\psi_{-4})$	-6.81	0	$0.71 -4\rangle + 0.71 +4\rangle$
$\varphi_2(\psi_{+4})$	-6.81	0	$0.71 -4\rangle - 0.71 +4\rangle$
$\varphi_3(\psi_{-3})$	-1.14	-3	$ -3\rangle$
$\varphi_4(\psi_{+3})$	-1.14	+3	$ +3\rangle$
$\varphi_5(\psi_{-2})$	1.44	0	$0.71 -2\rangle + 0.71 +2\rangle$
$\varphi_6(\psi_{+2})$	1.49	0	$0.71 -2\rangle - 0.71 +2\rangle$
$\varphi_7(\psi_{-1})$	3.95	-1	$ -1\rangle$
$\varphi_8(\psi_{+1})$	3.95	1	$ +1\rangle$
$\varphi_9(\psi_0)$	5.08	0	$ 0\rangle$

According to the simplified CF Hamiltonian (10) and  $\text{MAE}_{\text{DFT}} = 10.91$  meV, we immediately deduced  $D = -0.68$  meV,  $B_2^0 = -0.227$  meV, and  $E_{sf} = 4.77$  meV, respectively. In terms of the four-fold ligand field, the eigenstates should be the superpositions of pure  $J_z$  state separated by  $\Delta J_z = 4$ . With the derived  $B_n^k$  parameters of  $B_2^0 = -237$   $\mu\text{eV}$ ,  $B_4^0 = -1.03$   $\mu\text{eV}$ ,  $B_6^0 = -18$  neV,  $B_4^4 = 0.3$   $\mu\text{eV}$ , and  $B_6^4 = 13$  neV from the Table S6 within the Supplemental Material [88], we found that the energy spectrum morphology and the value of TZFS ( $\text{MAE} = 11.67$  meV) are consistent with the multiplet simulated results showed in Fig. 11(b), but greater value of  $E_{sf} = 7.61$  meV was actually acquired (Table S9 within the Supplemental Material [88]). To eliminate this difference,  $B_4^0$  was scaled by 0.1 and other parameters remain unchanged. Hence, we obtained the numerical solutions of nine eigenstates in compositions of the  $J_z$  states and labeled them orderly as  $\varphi_n$  ( $n = 1-9$ ) in Table VIII.

The nondiagonal Stevens operators of  $B_4^4 O_4^4$  and  $B_6^4 O_6^4$  terms give the remarkable mixtures, i.e.,  $|J_z = \pm 4\rangle$  in the  $\varphi_{1,2}$  eigenstates and  $|J_z = \pm 2\rangle$  in  $\varphi_{5,6}$  eigenstates, respectively. The pairwise-degenerate eigenstates have the symmetric and antisymmetric function forms within the same superpositions yet the opposite signs at opposite sides of the  $J_z$  barrier. Typically, equal coefficients of superposition  $J_z$  in  $\varphi_{1,2}$  and  $\varphi_{5,6}$  eigenstates lead to the quenched  $\langle J_z \rangle = 0$ . Others such as  $\varphi_{3,4,7,8,9}$  eigenstates are nearly pure  $J_z$  states, i.e.,  $\varphi_{3,4} = |J_z = \pm 3\rangle$ ,  $\varphi_{7,8} = |J_z = \pm 1\rangle$ , and  $\varphi_9 = |J_z = 0\rangle$ . In addition, we derived four groups of degenerate eigenvalues and one nondegenerate eigenvalue in Table VIII:  $\varepsilon_{1,2} = -6.81$  meV,  $\varepsilon_{3,4} = -1.14$  meV,  $\varepsilon_5 = 1.44$  meV,  $\varepsilon_6 = 1.49$  meV,  $\varepsilon_{7,8} = 3.95$  meV,  $\varepsilon_9 = 5.08$  meV, respectively. These findings are consistent with the multiplet simulation results not only for the superpositions of  $|J_z = \pm 4\rangle$  state with nearly equal weights but also for the energy level distribution.

We plotted the energy spectrum with the corresponding eigenstates in Fig. 12(a), and found that the induced TZFS = 11.89 meV ("ideal" MAE) are close to that of our DFT calculations. Concerning the possible QTM among the eigenstates within  $\Delta m_j = 4m$ , nine eigenstates were classified into four classes:  $\varphi_{1,2,9}$ ,  $\varphi_{3,8}$ ,  $\varphi_{5,6}$ , and  $\varphi_{4,7}$ , which are marked by pink, azure, green, and yellow colors in Fig. 12(b), respectively. The ground states  $\varphi_{1,2}$  and the second excited states

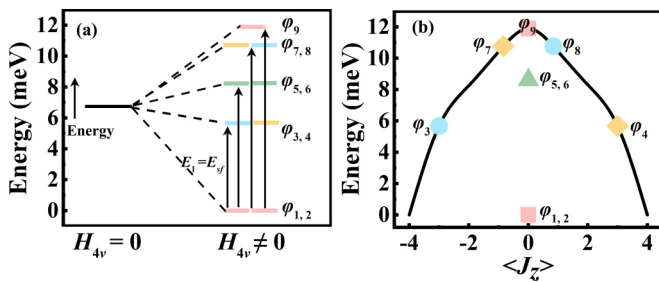


FIG. 12. Same as in Fig. 7 but for Nd adatom with Hamiltonian  $H_{4v}^{\text{Nd}}$ . Four mixture states of  $\varphi_{1,2}$  and  $\varphi_{5,6}$  at  $\langle J_z \rangle = 0$  depict the effect of transverse term  $B_4^4$  in mixing  $J_z = \pm 4, \pm 2$  components to form four singlet states with no net magnetization.

$\varphi_{5,6}$  are particularly delicate as they can be mixed by  $B_4^4 O_4^4$  operators, allowing the direct QTM due to the nonzero matrix elements  $\langle J_z = \mp 4 | (J_-^4 + J_+^4) | J_z = \mp 4 \rangle$  and  $\langle J_z = \pm 2 | (J_-^4 + J_+^4) | J_z = \mp 2 \rangle$ , respectively. Thus, the mixing of  $|J_z = \mp 4\rangle$  produces a doublet states with almost quenched  $\langle J_z \rangle = 0$ . The so-called Kondo case [101] would result in fast reversed magnetization and poor magnetic stability for Nd@MgO/Ag(100) system.

#### IV. CONCLUSIONS

In conclusion, we have employed the DFT method, multiplet simulation, and CF model Hamiltonians to investigate the individual Ce and Nd adatoms on thin insulating film grown on a conductive Ag(100) substrate for their magnetic stabilities of the ground states by inspecting the magnetic reversal. By making use of the DFT electronic structure analyses such as the deformation charge density, Mulliken charge and PDOS, we revealed the origins of MAE, magnetic moment, and bonding interactions, and found the magnetization

from both the  $5d$  conduction electrons and  $4f$  moments. Based on the simulated XAS and XMCD spectrum as well as the energy diagram of the magnetic states, we determined the ground-state doublets of pure  $|J = 5/2, J_z = \pm 5/2\rangle$  states and mixing states within  $|J = 4, J_z = \pm 4\rangle$  for Ce and Nd adatom, respectively. The effective magnetization reversal barrier of 2.87 meV with long magnetic lifetime about 239 s at 10 K was proposed for Ce adatom, while the poor magnetic stability with fast reversed magnetization was predicted for Nd atom. To outline the strategy achieving stable magnetization of Ln adatoms, we highlighted the suitable level scheme within large  $U_{\text{rev}}$  barrier and emphasized the QTM and spin-flip transitions on the dependence of angular momentum  $J$  with the matched CF symmetry. For Ce adatom on MgO substrate, high adsorption stability and high magnetic stability with long relaxation time demonstrate that it can possibly be synthesized and its magnetic ground state is expected to be read and written in experiments. Our surface-supported Ln adatoms represent model systems for the quantum magnetic storage and provide a reference method for future theoretical developments.

#### ACKNOWLEDGMENTS

This work was supported by the National Natural Science Foundation of China (Grants No. 12174320, and No. 22176181, and No. 11874306), the Natural Science Foundation of Chongqing, China (Grants No. cstc2021jcyj-msxmX0209 and No. cstc2022ycjh-bgzxm0127) and the Foundation of President of China Academy of Engineering Physics (Grant No. YZJJZQ2022011). We sincerely thank Harald Brune from École Polytechnique Fédérale de Lausanne and Fabio Donati from Institute for Basic Science for discussing the Multiplet Simulations.

All authors declare that they have no conflicts of interest.

- [1] P. Gambardella, S. Rusponi, M. Veronese, S. S. Dhesi, C. Grazioli, A. Dallmeyer, I. Cabria, R. Zeller, P. H. Dederichs, K. Kern *et al.*, Giant magnetic anisotropy of single cobalt atoms and nanoparticles, *Science* **300**, 1130 (2003).
- [2] A. A. Khajetoorians, B. Baxevanis, C. Hübner, T. Schlenk, S. Krause, T. O. Wehling, S. Lounis, A. Lichtenstein, D. Pfannkuche, J. Wiebe, and R. Wiesendanger, Current-driven spin dynamics of artificially constructed quantum magnets, *Science* **339**, 55 (2013).
- [3] I. G. Rau, S. Baumann, S. Rusponi, F. Donati, S. Stepanow, L. Gragnaniello, J. Dreiser, C. Piamonteze, F. Nolting, S. Gangopadhyay *et al.*, Reaching the magnetic anisotropy limit of a  $3d$  metal atom, *Science* **344**, 988 (2014).
- [4] T. Miyamachi, T. Schuh, T. Märkl, C. Bresch, T. Balashov, A. Stöhr, C. Karlewski, S. André, M. Marthaler, M. Hoffmann *et al.*, Stabilizing the magnetic moment of single holmium atoms by symmetry, *Nature (London)* **503**, 242 (2013).
- [5] F. Donati, S. Rusponi, S. Stepanow, C. Wäckerlin, A. Singha, L. Persichetti, R. Baltic, K. Diller, F. Patthey, E. Fernandes *et al.*, Magnetic remanence in single atoms, *Science* **352**, 318 (2016).
- [6] F. D. Natterer, K. Yang, W. Paul, P. Willke, T. Choi, T. Greber, A. J. Heinrich, and C. P. Lutz, Reading and writing single-atom magnets, *Nature (London)* **543**, 226 (2017).
- [7] R. Baltic, M. Pivetta, F. Donati, C. Wäckerlin, A. Singha, J. Dreiser, S. Rusponi, and H. Brune, Superlattice of single atom magnets on graphene, *Nano Lett.* **16**, 7610 (2016).
- [8] A. Singha, F. Donati, C. Wäckerlin, R. Baltic, J. Dreiser, M. Pivetta, S. Rusponi, and H. Brune, Magnetic hysteresis in Er trimers on Cu(111), *Nano Lett.* **16**, 3475 (2016).
- [9] R. Baltic, F. Donati, A. Singha, C. Wäckerlin, J. Dreiser, B. Delley, M. Pivetta, S. Rusponi, and H. Brune, Magnetic properties of single rare-earth atoms on graphene/Ir(111), *Phys. Rev. B* **98**, 024412 (2018).
- [10] F. Donati, M. Pivetta, C. Wolf, A. Singha, C. Wäckerlin, R. Baltic, E. Fernandes, J.-G. de Groot, S. L. Ahmed, L. Persichetti *et al.*, Correlation between electronic configuration and magnetic stability in dysprosium single atom magnets, *Nano Lett.* **21**, 8266 (2021).
- [11] F. Delgado and J. Fernández-Rossier, Storage of Classical Information in Quantum Spins, *Phys. Rev. Lett.* **108**, 196602 (2012).

- [12] F. Delgado and J. Fernández-Rossier, Spin decoherence of magnetic atoms on surfaces, *Prog. Surf. Sci.* **92**, 40 (2017).
- [13] F. Delgado, S. Loth, M. Zielinski, and J. Fernández-Rossier, The emergence of classical behaviour in magnetic adatoms, *Europhys. Lett.* **109**, 57001 (2015).
- [14] F. Delgado and J. Fernández-Rossier, RKKY oscillations in the spin relaxation rates of atomic-scale nanomagnets, *Phys. Rev. B* **95**, 075413 (2017).
- [15] F. Delgado and J. Fernández-Rossier, Enhanced lifetimes of spin chains coupled to chiral edge states, *New J. Phys.* **21**, 043008 (2019).
- [16] F. Donati, S. Rusponi, S. Stepanow, L. Persichetti, A. Singha, D. M. Juraschek, C. Wäckerlin, R. Baltic, M. Pivetta, K. Diller, C. Nistor, J. Dreiser, K. Kummer, E. Velez-Fort, N. A. Spaldin, H. Brune, and P. Gambardella, Unconventional Spin Relaxation Involving Localized Vibrational Modes in Ho Single-Atom Magnets, *Phys. Rev. Lett.* **124**, 077204 (2020).
- [17] J. Hu, P. Wang, J. Zhao, and R. Wu, Engineering magnetic anisotropy in two-dimensional magnetic materials, *Adv. Phys.: X* **3**, 1432415 (2018).
- [18] H. Brune and P. Gambardella, Magnetism of individual atoms adsorbed on surfaces, *Surf. Sci.* **603**, 1812 (2009).
- [19] M. Martins and W. Wurth, Magnetic properties of supported metal atoms and clusters, *J. Phys.: Condens. Matter* **28**, 503002 (2016).
- [20] A. A. Khajetoorians, T. Schlenk, B. Schweflinghaus, M. dos Santos Dias, M. Steinbrecher, M. Bouhassoune, S. Lounis, J. Wiebe, and R. Wiesendanger, Spin Excitations of Individual Fe Atoms on Pt(111): Impact of the Site-Dependent Giant Substrate Polarization, *Phys. Rev. Lett.* **111**, 157204 (2013).
- [21] Q. Dubout, F. Donati, C. Wäckerlin, F. Calleja, M. Etzkorn, A. Lehnert, L. Claude, P. Gambardella, and H. Brune, Controlling the Spin of Co Atoms on Pt(111) by Hydrogen Adsorption, *Phys. Rev. Lett.* **114**, 106807 (2015).
- [22] B. Schweflinghaus, M. dos Santos Dias, and S. Lounis, Observing spin excitations in 3d transition-metal adatoms on Pt(111) with inelastic scanning tunneling spectroscopy: A first-principles perspective, *Phys. Rev. B* **93**, 035451 (2016).
- [23] M. Kozanecki and C. Rudowicz, Importance of the fourth-rank zero field splitting parameters for  $\text{Fe}^{2+}$  ( $S = 2$ ) adatoms on the CuN/Cu(100) surface evidenced by their determination based on DFT and experimental data, *Phys. Chem. Chem. Phys.* **22**, 19837 (2020).
- [24] E. Fernandes, F. Donati, F. Patthey, S. Stavrić, Ž. Šljivančanin, and H. Brune, Adsorption sites of individual metal atoms on ultrathin MgO(100) films, *Phys. Rev. B* **96**, 045419 (2017).
- [25] O. R. Albertini, A. Y. Liu, and B. A. Jones, Site-dependent magnetism of Ni adatoms on MgO/Ag(001), *Phys. Rev. B* **91**, 214423 (2015).
- [26] H. Garai-Marin, J. I. Azpiroz, P. G. Goiricelaya, I. G. Gurtubay, and A. Eiguren, Electron-phonon coupling of Fe-adatom electron states on MgO/Ag(100), *Phys. Rev. B* **104**, 195422 (2021).
- [27] B. Shao, W. J. Shi, M. Feng, and X. Zuo, Large perpendicular magnetic anisotropy of single Co atom on MgO monolayer: A first-principles study, *J. Appl. Phys.* **117**, 17B316 (2015).
- [28] S. Baumann, W. Paul, T. Choi, C. P. Lutz, A. Ardavan, and A. J. Heinrich, Electron paramagnetic resonance of individual atoms on a surface, *Science* **350**, 417 (2015).
- [29] F. Donati, L. Gragnaniello, A. Cavallin, F. D. Natterer, Q. Dubout, M. Pivetta, F. Patthey, J. Dreiser, C. Piamonteze, S. Rusponi, and H. Brune, Tailoring the Magnetism of Co Atoms on Graphene through Substrate Hybridization, *Phys. Rev. Lett.* **113**, 177201 (2014).
- [30] S. K. Panda, I. Di Marco, O. Grånäs, O. Eriksson, and J. Fransson, Electronic and magnetic properties of single Fe atoms on a CuN surface: Effects of electron correlations, *Phys. Rev. B* **93**, 140101(R) (2016).
- [31] S. Siculo, L. Giordano, and G. Pacchioni, Adsorption of late transition metal atoms on MgO/Mo(100) and MgO/Ag(100) ultrathin films: A comparative DFT study, *J. Phys. Chem. C* **113**, 16694 (2009).
- [32] S. Loth, M. Etzkorn, C. P. Lutz, D. M. Eigler, and A. J. Heinrich, Measurement of fast electron spin relaxation times with atomic resolution, *Science* **329**, 1628 (2010).
- [33] B. Bryant, A. Spinelli, J. J. T. Wagenaar, M. Gerrits, and A. F. Otte, Local Control of Single Atom Magnetocrystalline Anisotropy, *Phys. Rev. Lett.* **111**, 127203 (2013).
- [34] M. Etzkorn, C. F. Hirjibehedin, A. Lehnert, S. Ouazi, S. Rusponi, S. Stepanow, P. Gambardella, C. Tieg, P. Thakur, A. I. Lichtenstein, A. B. Shick, S. Loth, A. J. Heinrich, and H. Brune, Comparing XMCD and DFT with STM spin excitation spectroscopy for Fe and Co adatoms on  $\text{Cu}_2\text{N}/\text{Cu}(100)$ , *Phys. Rev. B* **92**, 184406 (2015).
- [35] S. Baumann, F. Donati, S. Stepanow, S. Rusponi, W. Paul, S. Gangopadhyay, I. G. Rau, G. E. Pacchioni, L. Gragnaniello, M. Pivetta, J. Dreiser, C. Piamonteze, C. P. Lutz, R. M. Macfarlane, B. A. Jones, P. Gambardella, A. J. Heinrich, and H. Brune, Origin of Perpendicular Magnetic Anisotropy and Large Orbital Moment in Fe Atoms on MgO, *Phys. Rev. Lett.* **115**, 237202 (2015).
- [36] N. Lorente and J.-P. Gauyacq, Efficient Spin Transitions in Inelastic Electron Tunneling Spectroscopy, *Phys. Rev. Lett.* **103**, 176601 (2009).
- [37] J. Fernández-Rossier, Theory of Single-Spin Inelastic Tunneling Spectroscopy, *Phys. Rev. Lett.* **102**, 256802 (2009).
- [38] J. Fransson, Spin inelastic electron tunneling spectroscopy on local spin adsorbed on surface, *Nano Lett.* **9**, 2414 (2009).
- [39] N. Reyren, S. Thiel, A. D. Caviglia, L. Fitting Kourkoutis, G. Hammerl, C. Richter, C. W. Schneider, T. Kopp, A.-S. Rüetschi, D. Jaccard *et al.*, Superconducting interfaces between insulating oxides, *Science* **317**, 1196 (2007).
- [40] W. Paul, K. Yang, S. Baumann, N. Romming, T. Choi, C. P. Lutz, and A. J. Heinrich, Control of the millisecond spin lifetime of an electrically probed atom, *Nat. Phys.* **13**, 403 (2017).
- [41] A. B. Shick and A. I. Lichtenstein, Electronic structure and magnetic properties of Dy adatom on Ir surface, *J. Magn. Magn. Mater.* **454**, 61 (2018).
- [42] K. C. Zhang, Y. F. Li, Y. Liu, Y. Zhu, and L. B. Shi, Giant magnetic anisotropy of rare-earth adatoms and dimers adsorbed by graphene oxide, *Phys. Chem. Chem. Phys.* **19**, 13245 (2017).
- [43] T. Balashov, C. Karlewski, T. Märkl, G. Schön, and W. Wulfhekel, Electron-assisted magnetization tunneling in single spin systems, *Phys. Rev. B* **97**, 024412 (2018).
- [44] A. B. Shick and A. Y. Denisov, Magnetism of 4f-atoms adsorbed on metal and graphene substrates, *J. Magn. Magn. Mater.* **475**, 211 (2019).



- [45] M. Karbowski and C. Rudowicz, Ground state of Ho atoms on Pt(111) metal surfaces: Implications for magnetism, *Phys. Rev. B* **93**, 184415 (2016).
- [46] C. Karlewski, M. Marthaler, T. Märkl, T. Balashov, W. Wulfhekel, and G. Schön, Magnetic adatoms as memory bits: A quantum master equation analysis, *Phys. Rev. B* **91**, 245430 (2015).
- [47] T. Schuh, T. Miyamachi, S. Gerstl, M. Geilhufe, M. Hoffmann, S. Ostanin, W. Hergert, A. Ernst, and W. Wulfhekel, Magnetic excitations of rare earth atoms and clusters on metallic surfaces, *Nano Lett.* **12**, 4805 (2012).
- [48] M. Marciari, C. Hübner, and B. Baxevanis, General scheme for stable single and multiatom nanomagnets according to symmetry selection rules, *Phys. Rev. B* **95**, 125433 (2017).
- [49] M. Steinbrecher, A. Sonntag, M. dos Santos Dias, M. Bouhassoune, S. Lounis, J. Wiebe, R. Wiesendanger, and A. A. Khajetoorians, Absence of a spin-signature from a single Ho adatom as probed by spin-sensitive tunneling, *Nat. Commun.* **7**, 10454 (2016).
- [50] P. R. Forrester, F. Patthey, E. Fernandes, D. P. Sblendorio, H. Brune, and F. D. Natterer, Quantum state manipulation of single atom magnets using the hyperfine interaction, *Phys. Rev. B* **100**, 180405(R) (2019).
- [51] F. D. Natterer, F. Donati, F. Patthey, and H. Brune, Thermal and Magnetic-Field Stability of Holmium Single-Atom Magnets, *Phys. Rev. Lett.* **121**, 027201 (2018).
- [52] A. Singha, F. Donati, F. D. Natterer, C. Wäckerlin, S. Stavrić, Z. S. Popović, Ž. Šljivančanin, F. Patthey, and H. Brune, Spin Excitations in a  $4f - 3d$  Heterodimer on MgO, *Phys. Rev. Lett.* **121**, 257202 (2018).
- [53] A. Singha, D. Sostina, C. Wolf, S. L. Ahmed, D. Krylov, L. Colazzo, P. Gargiani, S. Agrestini, W.-S. Noh, J.-H. Park *et al.*, Mapping orbital-resolved magnetism in single lanthanide atoms, *ACS Nano* **15**, 16162 (2021).
- [54] A. Chiesa, F. Cugini, R. Hussain, E. Macaluso, G. Allodi, E. Garlatti, M. Giansiracusa, C. A. P. Goodwin, F. Ortu, D. Reta, J. M. Skelton, T. Guidi, P. Santini, M. Solzi, R. De. Renzi, D. P. Mills, N. F. Chilton, and S. Carretta, Understanding magnetic relaxation in single-ion magnets with high blocking temperature, *Phys. Rev. B* **101**, 174402 (2020).
- [55] A. Singha, P. Willke, T. Bilgeri, X. Zhang, H. Brune, F. Donati, A. J. Heinrich, and T. Choi, Engineering atomic-scale magnetic fields by dysprosium single atom magnets, *Nat. Commun.* **12**, 4179 (2021).
- [56] S. Schumacher, F. Huttmann, M. Petrović, C. Witt, D. F. Förster, C. Vo-Van, J. Coraux, A. J. Martínez-Galera, V. Sessi, I. Vergara, R. Rückamp, M. Grüninger, N. Schleheck, F. M. zu Heringdorf, P. Ohresser, M. Kralj, T. O. Wehling, and T. Michely, Europium underneath graphene on Ir(111): Intercalation mechanism, magnetism, and band structure, *Phys. Rev. B* **90**, 235437 (2014).
- [57] D. Mousadakos, M. Pivetta, H. Brune, and S. Rusponi, Sm cluster superlattice on graphene/Ir(111), *New J. Phys.* **19**, 123021 (2017).
- [58] M. Pivetta, F. Patthey, I. D. Marco, A. Subramonian, O. Eriksson, S. Rusponi, and H. Brune, Measuring the Intra-Atomic Exchange Energy in Rare-Earth Adatoms, *Phys. Rev. X* **10**, 031054 (2020).
- [59] A. B. Shick, J. Kolorenč, A. Yu. Denisov, and D. S. Shapiro, Magnetic anisotropy of a Dy atom on a graphene/Cu(111) surface, *Phys. Rev. B* **102**, 064402 (2020).
- [60] D. Coffey, C. de la Fuente, M. Ciria, D. Serrate, S. Loth, and J. I. Arnaudás, Mixed  $4f$  population of Tm adatoms on insulating  $\text{Cu}_2\text{N}$  islands, *Phys. Chem. Chem. Phys.* **22**, 196 (2020).
- [61] A. B. Shick, D. S. Shapiro, J. Kolorenč, and A. I. Lichtenstein, Magnetic character of holmium atom adsorbed on platinum surface, *Sci. Rep.* **7**, 2751 (2017).
- [62] C. Nistor, A. Mugarza, S. Stepanow, P. Gambardella, K. Kummer, J. L. Diez-Ferrer, D. Coffey, C. de la Fuente, M. Ciria, and J. I. Arnaudás, Structure and magnetism of Tm atoms and monolayers on W(110), *Phys. Rev. B* **90**, 064423 (2014).
- [63] A. Singha, R. Baltic, F. Donati, C. Wäckerlin, J. Dreiser, L. Persichetti, S. Stepanow, P. Gambardella, S. Rusponi, and H. Brune,  $4f$  occupancy and magnetism of rare-earth atoms adsorbed on metal substrates, *Phys. Rev. B* **96**, 224418 (2017).
- [64] C. N. M. Ouma, S. Singh, K. O. Obodo, G. O. Amolo, and A. H. Romero, Controlling the magnetic and optical responses of a  $\text{MoS}_2$  monolayer by lanthanide substitutional doping: A first-principles study, *Phys. Chem. Chem. Phys.* **19**, 25555 (2017).
- [65] M. Ternes, C. P. Lutz, A. J. Heinrich, and W. D. Schneider, Sensing the Spin of an Individual Ce Adatom, *Phys. Rev. Lett.* **124**, 167202 (2020).
- [66] J. P. Perdew, K. Burke, and M. Ernzerhof, Generalized Gradient Approximation Made Simple, *Phys. Rev. Lett.* **77**, 3865 (1996).
- [67] T. Ozaki, Variationally optimized atomic orbitals for large-scale electronic structures, *Phys. Rev. B* **67**, 155108 (2003).
- [68] T. Ozaki and H. Kino, Numerical atomic basis orbitals from H to Kr, *Phys. Rev. B* **69**, 195113 (2004).
- [69] T. Ozaki and H. Kino, Efficient projector expansion for the *ab initio* LCAO method, *Phys. Rev. B* **72**, 045121 (2005).
- [70] H. J. Monkhorst and J. D. Pack, Special points for Brillouin-zone integrations, *Phys. Rev. B* **13**, 5188 (1976).
- [71] M. Cococcioni and S. de Gironcoli, Linear response approach to the calculation of the effective interaction parameters in the LDA+U method, *Phys. Rev. B* **71**, 035105 (2005).
- [72] M. Topsakal and R. M. Wentzcovitch, Accurate projected augmented wave (PAW) datasets for rare-earth elements (RE = La - Lu), *Comput. Mater. Sci.* **95**, 263 (2014).
- [73] P. Larson, W. R. L. Lambrecht, A. Chantis, and M. van Schilfhaarde, Electronic structure of rare-earth nitrides using the LSDA+U approach: Importance of allowing  $4f$  orbitals to break the cubic crystal symmetry, *Phys. Rev. B* **75**, 045114 (2007).
- [74] S. Grimme, Semiempirical GGA-Type density functional constructed with a long-range dispersion correction, *J. Comput. Chem.* **27**, 1787 (2006).
- [75] A. Uldry, F. Vernay, and B. Delley, Systematic computation of crystal-field multiplets for x-ray core spectroscopies, *Phys. Rev. B* **85**, 125133 (2012).
- [76] N. F. Chilton, D. Collison, E. J. L. McInnes, R. E. P. Winpenney, and A. Soncini, An electrostatic model for the determination of magnetic anisotropy in dysprosium complexes, *Nat. Commun.* **4**, 2551 (2013).

- [77] B. G. Wybourne, Effective operators and spectroscopic properties, *J. Chem. Phys.* **48**, 2596 (1968).
- [78] I. D. Ryabov, On the operator equivalents and the crystal-field and spin hamiltonian parameters, *Appl. Magn. Reson.* **35**, 481 (2009).
- [79] T. Balashov, T. Miyamachi, T. Schuh, T. Märkl, C. Bresch, and W. Wulfhekel, Dynamic magnetic excitations in  $3d$  and  $4f$  atoms and clusters, *Surf. Sci.* **630**, 331 (2014).
- [80] B. Bleaney and K. W. H. Stevens, Paramagnetic resonance, *Rep. Prog. Phys.* **16**, 108 (1953).
- [81] S. K. Misra, C. P. Poole, and H. A. Farach, A review of spin hamiltonian forms for various point-group site symmetries, *Appl. Magn. Reson.* **11**, 29 (1996).
- [82] R. Giraud, W. Wernsdorfer, A. M. Tkachuk, D. Maily and B. Barbara, Nuclear Spin Driven Quantum Relaxation in  $\text{LiY}_{0.998}\text{Ho}_{0.002}\text{F}_4$ , *Phys. Rev. Lett.* **87**, 057203 (2001).
- [83] Z. Mazurak, A. Garcia, and C. Fouassier, Luminescence spectra and crystal field analysis of LaOBr doped with  $\text{Tm}^{3+}$ , *J. Phys.: Condens. Matter* **6**, 2031 (1994).
- [84] C. F. Hirjibehedin, C. Y. Lin, A. F. Otte, M. Ternes, C. P. Lutz, B. A. Jones, and A. J. Heinrich, Large magnetic anisotropy of a single atomic spin embedded in a surface molecular network, *Science* **317**, 1199 (2007).
- [85] T. Schuh, T. Balashov, T. Miyamachi, S. Y. Wu, C. C. Kuo, A. Ernst, J. Henk, and W. Wulfhekel, Magnetic anisotropy and magnetic excitations in supported atoms, *Phys. Rev. B* **84**, 104401 (2011).
- [86] L. Thomas, F. Lioni, R. Ballou, D. Gatteschi, R. Sessoli, and B. Barbara, Macroscopic quantum tunnelling of magnetization in a single crystal of nanomagnets, *Nature (London)* **383**, 145 (1996).
- [87] X. J. Liu, C. Z. Wang, M. Hupalo, Y. X. Yao, M. C. Tringides, W. C. Lu, and K. M. Ho, Adsorption and growth morphology of rare-earth metals on graphene studied by *ab initio* calculations and scanning tunneling microscopy, *Phys. Rev. B* **82**, 245408 (2010).
- [88] See Supplemental Material at <http://link.aps.org/supplemental/10.1103/PhysRevB.107.214444> for the detail data of point charge position and strength, energy levels, eigenvalues and eigenvectors,  $\langle L_z \rangle$ ,  $\langle S_z \rangle$ , and  $\langle J_z \rangle$  expectation values of Ce, Nd adsorbed on the MgO/Ag(100) surface. The material also contains Refs. [5,28,35,80,98].
- [89] C. O. Rodriguez, M. V. Ganduglia-Pirovano, E. L. Peltzer y Blancá, M. Petersen, and P. Novák, Orbital and dipolar contributions to the hyperfine fields in bulk bcc Fe, hcp Co, and at the Fe/Ag(100) interface: The inclusion of orbital polarization, *Phys. Rev. B* **63**, 184413 (2001).
- [90] J. D. Rinehart and J. R. Long, Exploiting single-ion anisotropy in the design of f-element single-molecule magnets, *Chem. Sci.* **2**, 2078 (2011).
- [91] D. S. Wang, R. Q. Wu, and A. J. Freeman, First-principles theory of surface magnetocrystalline anisotropy and the diatomic-pair model, *Phys. Rev. B* **47**, 14932 (1993).
- [92] G. Pacchioni and H. Freund, Electron transfer at oxide surfaces. The MgO paradigm: From defects to ultrathin films, *Chem. Rev.* **113**, 4035 (2013).
- [93] B. T. Thole, G. van der Laan, J. C. Fuggle, G. A. Sawatzky, R. C. Karnatak, and J.-M. Esteve,  $3d$  x-ray-absorption lines and the  $3d^{94}f^{n+1}$  multiplets of the lanthanides, *Phys. Rev. B* **32**, 5107 (1985).
- [94] F. Huttmann, D. Klar, N. Atodiresei, C. S. Antoniak, and A. Smekhova, Magnetism in a graphene- $4f$ - $3d$  hybrid system, *Phys. Rev. B* **95**, 075427 (2017).
- [95] J. B. Goedkoop, B. T. Thole, G. van der Laan, G. A. Sawatzky, F. M. F. de Groot, and J. C. Fuggle, Calculations of magnetic x-ray dichroism in the  $3d$  absorption spectra of rare-earth compounds, *Phys. Rev. B* **37**, 2086 (1988).
- [96] F. Donati, A. Singha, S. Stepanow, C. Wäckerlin, J. Dreiser, P. Gambardella, S. Rusponi, and H. Brune, Magnetism of Ho and Er Atoms on Close-Packed Metal Surfaces, *Phys. Rev. Lett.* **113**, 237201 (2014).
- [97] M. Richter, P. M. Oppeneer, H. Eschrig, and B. Johansson, Calculated crystal-field parameters of  $\text{SmCo}_5$ , *Phys. Rev. B* **46**, 13919 (1992).
- [98] A. J. Freeman and R. E. Watson, Theoretical investigation of some magnetic and spectroscopic properties of rare-earth ions, *Phys. Rev.* **127**, 2058 (1962).
- [99] C. Görrler-Walrand and K. Binnemans, Rationalization of crystal-field parametrization, in *Handbook on the Physics and Chemistry of Rare Earths*, edited by J. K. A. Gschneidner and L. Eyring (North-Holland, Amsterdam, 1996), Vol. 23, p. 121.
- [100] A. L. Kozub, A. B. Shick, F. Maca, J. Kolorenc, and A. I. Lichtenstein, Electronic structure and magnetism of samarium and neodymium adatoms on free-standing graphene, *Phys. Rev. B* **94**, 125113 (2016).
- [101] H. Chen, T. Frauhammer, S. Sasaki, T. K. Yamada, and W. Wulfhekel, Interplay between point symmetry, oxidation state, and the Kondo effect in  $3d$  transition metal acetylacetonate molecules on Cu(111), *Phys. Rev. B* **103**, 085423 (2021).